

# The soft X-ray emission in a large sample of galaxy clusters with ROSAT PSPC

Massimiliano Bonamente<sup>1,2</sup>, Richard Lieu<sup>1</sup>, Marshall K. Joy<sup>2</sup> and Jukka H. Nevalainen<sup>1</sup>

<sup>1</sup>*Department of Physics, University of Alabama, Huntsville, AL*

<sup>2</sup>*NASA Marshall Space Flight Center, Huntsville, AL*

## ABSTRACT

The study of soft X-ray emission of 38 X-ray selected galaxy clusters observed by *ROSAT* PSPC indicates that the *soft excess* phenomenon may be a common occurrence in galaxy clusters. Excess soft X-ray radiation, above the contribution from the hot intra-cluster medium, is evident in a large fraction of sources, and is clearly detected with large statistical significance in the deepest observations. The investigation relies on new, high resolution 21 cm HI observations. The sample selection also features analysis of infra-red images, to further ensure reliability of results with respect to the characteristics of Galactic absorption. The possibility of background or calibration effects as cause of the excess emission is likewise investigated; a detailed analysis of the distribution of the excess emission with respect to detector position and Galactic HI column density shows that the excess emission is a genuine celestial phenomenon. We find evidence for a preferential distribution of the soft excess emission at distances larger than  $\sim 150 - 200$  kpc from the centers of clusters; this behavior may be naturally explained in the context of a non-thermal Inverse-Compton scenario. Alternatively, we propose that the phenomenon may be caused by thermal emission of very large-scale ‘warm’ filaments seen in recent hydrodynamic simulations. This new interpretation relieves the very demanding requirements of either the traditional intra-cluster ‘warm’ gas and the non-thermal scenarios. We also investigate the possibility of the soft excess originating from unresolved, X-ray faint cluster galaxies.

## 1. Introduction

Clusters of galaxies are strong emitters of X-rays, which originate from a very diffuse and hot phase of the intra-cluster medium (ICM). At the typical temperatures of  $T \sim 1-10 \times 10^7$  K, the bulk of the hot ICM radiation is detected near energies of 1 keV and above;

intervening Galactic absorption is responsible for a substantial reduction of flux below  $\sim 1$  keV.

The soft X-ray band around 0.25 keV (hereafter C-band) offers a unique window to investigate the presence of other emitting/absorbing phases of the ICM. The initial discovery of soft X-ray and extreme ultra-violet (EUV) excess emission in a few nearby galaxy clusters with the *Extreme Ultra-Violet Explorer* and *ROSAT* missions (Coma, Virgo, A2199, A1795; Lieu et al. 1996a,b; Mittaz, Lieu and Lockman 1998; Lieu, Bonamente and Mittaz 1999) was soon followed by many re-observations and re-analyses of the same objects, plus a few more clusters, with the aid of complementary data from *BeppoSAX*, *Far Ultraviolet Spectroscopic Explorer*, *Rossi X-Ray Timing Explorer* and *Hopkins Ultraviolet Telescope* (Fabian 1996; Bonamente, Lieu and Mittaz 2001b; Bonamente et al. 2001c; Lieu et al. 1999b, 1999c; Berghoefer, Bowyer and Korpela 2000a, 2000b; Bowyer and Berghoefer 1998; Bowyer and Berghoefer 2001; Bowyer, Berghoefer and Korpela 1999; Arabadjis and Bregman 1999; Reynolds et al. 1999; Kaastra et al. 1999; Dixon et al. 2001; Dixon, Hurwitz and Ferguson 1996; Valinia et al. 2000; Fusco-Femiano et al. 2000; Buote 2000a,2000b,20001; Arnaud et al. 2001). The present analysis of a very large sample of X-ray selected clusters has the primary aim of assessing the cosmological importance of this *soft excess* emission. It is also known that some clusters may harbor, at their centers, colder gas which absorbs the soft X-ray radiation (Fabian 1988). Recent XMM observations however did not detect large amounts of cold gas in the center of galaxy clusters (e.g., Boehringer et al. 2002), and our analysis of PSPC data shows soft X-ray absorption only in the minority of the sources.

The PSPC detector on board *ROSAT* is perfectly suited for studies of this kind. Along with a sizable effective area of  $\sim 150$  cm<sup>2</sup> at 0.25 keV, pulse invariant (PI) channels 20-41 ( $\sim 0.2$ - $0.4$  by photon energy) covering the C-band are stable and well calibrated (e.g., Snowden et al. 1994). The instrument, moreover, has a very low detector background, and conducted a large number of deep cluster observations throughout its lifetime. The large field of view of  $\sim 1$  degree radius permits also the use of *in situ* background measurements, necessary for the correct estimation and subtraction of the C-band background emission.

## 2. Sample selection

The sample of galaxy clusters we analyzed consists of the 38 clusters in Table 1, selected from all the clusters observed by the PSPC during its pointed phase, according to the following criteria:

- they are located at high Galactic latitude ( $\beta \geq 30$  degrees) and with a count rate  $\geq 0.2$

counts  $\text{s}^{-1}$  in 0.5-2.0 keV band (e.g., Schwobe et al. 2000). The high Galactic latitude portion of the sky avoids regions of strong  $N_H$  gradients along the Galactic plane;

- Galactic HI column density  $N_H \leq 5 \times 10^{20} \text{ cm}^{-2}$ , and availability of narrow beam HI measurement with resolution of  $\sim 20$  arcmin (Murphy et al., in prep.). The measurements of Murphy et al. (in prep.) with the 140-ft NRAO telescope at Green Bank constitute the best Galactic  $N_H$  data toward galaxy clusters to date (the Dickey and Lockman survey [Dickey and Lockman, 1990] has a resolution of  $\sim 1$  degree), with a beam-size comparable to the X-ray extent of the clusters;
- analysis of IRAS 100  $\mu\text{m}$  images (Wheelock et al. 1994) confirms smoothness of the Galactic absorbing gas distribution. It is in fact known that the 100  $\mu\text{m}$  emission correlates well with  $N_H$ , and IRAS maps can further detect asymmetries and gradients in the distribution of the Galactic absorbing material with a better resolution of approximately 3 arcmin.

With these conditions in place, the  $N_H$  toward the clusters, a primary parameter that ensures the accurate reconstruction of C-band signals, can be known with an uncertainty of less than  $1 \times 10^{19} \text{ cm}^{-2}$  (Murphy et al., in prep.). Moreover, given that through a column density of  $4 \times 10^{20} \text{ cm}^{-2}$  a 0.25 keV photon has an optical depth of  $\sim 4$ , we restricted our analysis to sources with  $N_H \leq 5 \times 10^{20} \text{ cm}^{-2}$ . Many rich and nearby clusters (e.g., A496, A4038, A2052 etc.) were not considered in this sample, because either a narrow beam  $N_H$  measurement was unavailable, or on account of their positional coincidence with a Galactic IR cirrus gradient. In addition, all clusters <sup>1</sup> have an X-ray angular extent of less than 1 degree radius, and local background can be obtained from the outer regions of the PSPC detector.

---

<sup>1</sup>With the only possible exceptions of Coma and Virgo, where marginal cluster emission may be present even near the detector edges. In these two clusters, analyzed only to a radius of 18 arcmin to minimize background effects, the background is estimated from the outermost detector regions, and amounts to  $\leq 20\%$  of the cluster signals at most. Even a  $\sim 50\%$  uncertainty on the background level results in a  $\leq 10\%$  effect on the soft excess fluxes, although the background is likely an overestimate which, in turn, underestimates the soft excess fluxes.

Table 1. Characteristics of galaxy clusters analyzed in this paper

Cluster	$z$	$N_H$ ( $10^{20}$ cm $^{-2}$ )	CF	$r_c$ (kpc)	Abell richness
A21	0.095	3.7	no [WJF97]	600 [W97]	1
A85	0.055	2.7	yes [WJF97]	317 [M99]	1
A133	0.057	1.5	yes [WJF97]	300 [W97]	0
A665	0.1816	4.3	no [WJF97]	1000 [W97]	5
A1045	0.138	1.4	...	240 [c]	0
A1068	0.139	1.57	yes [A00]	390 [E96]	0
A1302	0.116	1.0	...	330 [E96]	0
A1314	0.0341	1.6	no [WJF97]	500 [W97]	0
A1361	0.1167	2.5	yes [A95]	270 [E96]	0
A1367	0.0276	1.7	unc. [WFJ97,P98]	360 [M99]	2
A1413	0.143	1.71	no [WJF97]	500 [W97]	3
A1689	0.181	1.72	no [WJF97,P98]	131 [M99]	4
A1795	0.061	1.01	yes [WJF97]	344 [M99]	2
A1914	0.171	0.95	...	580 [E96]	2
A1991	0.0586	2.25	yes [WJF97]	200 [W97]	1
A2029	0.0767	3.2	yes [WJF97]	334 [M99]	2
A2142	0.09	4.15	yes [WJF97]	580 [HB96]	2
A2199	0.0302	0.85	yes [WJF97]	162 [M99]	2
A2218	0.171	2.75	unc. [WJF97,A00]	230 [NB99]	4
A2219	0.228	2.04	no [A00]	650 [E96]	0
A2241	0.0635	2.05	...	80 [c]	0
A2244	0.097	1.9	yes [WJF97]	117 [M99]	2
A2255	0.08	2.51	no [WJF97]	584 [M99]	2
A2256	0.06	4.55	no [WJF97]	486 [M99]	2
A2597	0.085	2.2	yes [A01]	44 [M99]	0
A2670	0.076	2.73	yes [WJF97]	600 [W97]	3
A2717	0.049	1.23	...	47 [L97]	1
A2744	0.308	1.41	no [A00]	1000 [E96]	3
A3301	0.054	2.49		140 [c]	3
A3558	0.048	4.0	yes [P98]	194 [M99]	4
A3560	0.04	4.7	...	170 [E96]	3

Table 1—Continued

Cluster	$z$	$N_H$ ( $10^{20}$ cm $^{-2}$ )	CF	$r_c$ (kpc)	Abell richness
A3562	0.04	4.01	no [WJF97]	97 [M99]	2
A3571	0.04	4.4	yes [P98]	173 [M99]	2
A4059	0.046	1.06	yes [WJF97]	78 [M99]	1
Coma (A1656)	0.023	0.9	no [WJF97]	386 [M99]	2
Fornax (AS373)	0.0046	1.5	yes [WJF97]	10 [W97]	0
Hercules (A2151)	0.037	3.2	yes [WJF97]	35 [HB99]	2
Virgo (M87)	0.0043	1.8	yes	300 [W97]	...

Note. — Clusters are ordered alphabetically,  $z$  is redshift,  $N_H$  is Galactic HI column density, CF indicates whether the source is believed to host cooler gas at its center,  $r_c$  is X-ray core radius.

References: WJF97 and W97 - White, Jones and Forman 1997; A00 - Allen 2000; A01 - Allen, Fabian, Johnstone, Arnaud and Nulsen 2001; A95 - Allen, Fabian, Edge, Boheringer and White 1995; P98 - Peres, Fabian, Edge, Allen, Johnston and White 1998; E96 - Ebeling et al. 1996; M99 - Mohr et al. 1999; HB96 - Henry and Briel 1996 (A2142) ; L97 - Liang et al. 1997 (2717); HS96 - Huang and Sarazin 1996 (Hercules) ; NB99 - Neumann and Boheringer 1999 (A2218) ; c - this work

Table 2. Log of PSPC observations. Nearly 570 ks of PSPC data was reduced and analyzed.

Cluster	Obs. ID	Obs. date	Exp. time (ks)
A21	800107	25/12/91	8.5
A85	800250	1/7/92	8.4
	800174a00	20/12/91	2.1
	800174a01	11/6/92	3.3
A133	800319	5/7/92	15.5
A665	800022	10/4/91	35.0
A1045	800350	28/5/93	9.1
A1068	800410	4/12/92	9.8
A1302	800260	29/9/92	2.3
A1314	800392	9/6/93	2.0
A1361	800412	7/6/93	3.9
A1367	800153	2/12/91	17.8
A1413	800183	27/11/91	14.3
A1689	800248	18/7/92	13.5
A1795	800055	1/7/91	25.0
	800105	4/1/92	35.0
A1914	800345	20/7/92	6.4
A1991	800518a01	4/8/93	20.9
	800294	8/8/92	2.8
A2029	800249	10/8/92	9.9
A2142	150084	20/7/90	7.5
	800096	25/8/92	5.9
	800233	26/8/92	4.8
A2199	150083	18/7/90	10.0
A2218	800097	25/5/91	36.4
A2219	800571	2/8/93	8.5
A2241	800530	3/8/93	9.9
A2244	800265	21/9/92	2.9
A2255	800512	5/9/93	14.5
A2256	100110	17/6/90	16.6
A2597	800112	27/11/91	6.7

### 3. Data and data analysis

The PSPC data were reduced according to the prescriptions of Snowden et al. (1994). The datasets, available through public archives (NASA’s W3Browse and the Leicester LEDAS databases) were corrected for detector gain fluctuations, and only events with Average Master Veto rate  $\leq 170 \text{ c s}^{-1}$  were considered, in order to discard periods of high particle background. The PSPC rejection efficiency for particle background is 99.9% in the energy range 0.2-2 keV (Plucinsky et al. 1993), and the background is therefore solely represented by the photonic component. After a ‘cleaned’ dataset was obtained, each observation was divided into a number of concentric annular regions between 2 and 8, according to the size and the brightness of each source; the linear size of each region was never less than 1 arcmin. Response files associated with the spectra account for the instrument’s point-spread function (PSF) and vignetting. Moreover, all obvious point sources were accurately removed.

The C-band background is dominated by the Galactic soft X-ray emission (e.g., Snowden et al. 1998). Owing to the large field of view of the PSPC, it is possible to measure the background from a peripheral detector region (typically an annular region near 40 arcmin from boresight) where cluster emission is negligible. A background spectrum is extracted for each dataset, and rescaled to each cluster region according to area, vignetting and the energy-dependent detector response at different detector positions (see also Bonamente et al. 2001c). This *in situ* background is the most accurate for the purpose of background subtraction, as it is taken at the same time as the cluster spectra, and at a minimal angular distance from the cluster’s position. Peripheral cluster regions are most affected by the background; regions where the cluster emission drops below 25% of the background can be considered as limiting radii of the C-band detection for each cluster. The integrity of the employed background subtraction technique is implied by the absence of excess emission/absorption in those regions where negligible cluster signal is detected (see next section).

Dedicated narrow-beam 21-cm observations are available from the NRAO 140-ft Green Bank telescope, with a resolution of  $\sim 20$  arcmin. They provide  $N_H$  measurements with an accuracy of less than  $1 \times 10^{19} \text{ cm}^{-2}$ , (Murphy et al., in prep.; see Table 2) for a large number of galaxy clusters. On occasions for which a comparison with stellar Ly $\alpha$  and quasar X-ray spectra could be made, the agreement among the different methods of determining  $N_H$  would again suggest an error of  $\leq 10^{19} \text{ cm}^{-2}$  (see Laor et al. 1994; Elvis, Lockman and Wilkes 1989; Dickey and Lockman 1990), irrelevant to the results of this study. In addition, IRAS 100  $\mu\text{m}$  maps (with a resolution of  $\sim 3$  arcmin) can give further constraints on the state and distribution of the Galactic absorbing material. In accordance with the  $N_H$ -IR correlation (with scaling factor of  $\sim 1.2 \times 10^{20} \text{ cm}^{-2} (\text{MJy sr}^{-1})^{-1}$ , Boulanger and Perault 1988), we checked that no strong IR gradients were present in a  $1 \times 1$  degree IRAS field around the

cluster, and that quantitatively the  $N_H$  toward the background region was consistent (to within a few  $10^{19} \text{ cm}^{-2}$ ) with that measured at the cluster position. When this check failed, the candidate was discarded from the sample. On the basis of this criterion, A496 and A500 are not considered here, as they both lay in a region of strong Galactic IR cirrus gradient.

The limited band and energy resolution of the PSPC instrument (0.2-2 keV) is not ideally suited for the determination of the hot ICM parameters (temperature  $T$  and metal abundance  $A$ ) of very hot clusters ( $T \geq 3\text{-}4 \text{ keV}$ ), although it is proven that deep PSPC observations can yield accurate temperature maps even for hot clusters (e.g., Henry and Briel 1996). To avoid the controversy, we employed the spatially resolved best-fit hot ICM parameters available elsewhere in the literature where  $kT \geq 3 - 4 \text{ keV}$  (see Table 3 for references); with  $kT$  and  $A$  fixed at their best fit, and  $N_H$  at the measured values, we fitted the PSPC 0.5-2 keV spectra to a photoabsorbed thin plasma emission model. The goodness of fit implies that 0.5-2 keV PSPC spectra are well described by the employed models. For those cluster regions where  $kT \leq 3\text{-}4 \text{ keV}$ , or those cases where literature values were unavailable, we fitted the hot ICM parameters to the 0.5-2 keV PSPC spectra. The reason for avoiding the 0.2-0.5 keV portion of the PSPC spectra to model the hot ICM emission is that such an undertaking enables us to study the C-band emission in an unbiased fashion. It is clear that, e.g., any excess emission in 0.2-0.4 keV band will result in a tendency of the hot ICM parameters toward lower  $kT$ , if the entire 0.2-2 keV spectrum is used for the fit of the hot ICM model <sup>2</sup>.

The optically thin emission code is MEKAL (in XSPEC language; Mewe, Gronenschild and van den Oord 1985; Mewe, Lemen and van den Oord 1986; Kaastra 1992), and Galactic absorption was modeled with the codes of Morrison and McCammon 1983 (WABS). The cross sections of WABS are in good agreement with the recent compilation of Yan, Saghdepour and Dalgarno (1998), as also shown in Bonamente, Lieu and Mittaz (2001b). The most up-to-date code by Wilms, Allen and McCray 2000 (TBABS) is virtually indistinguishable from WABS at the resolution of PSPC, and yield the same results (see Bonamente, Lieu and Mittaz 2001d).

Once a model of the hot ICM is obtained, detected C-band fluxes are compared with model predictions, see Table 3. The fractional excess/absorption function  $\eta$  is defined as

$$\eta = \frac{p - q}{q} \quad (1)$$

---

<sup>2</sup>This is in fact evident in the case of Sérsic 159-03, see Bonamente, Lieu and Mittaz (2001d), where the strong soft excess prevents a good fit to be found over the whole 0.2-2 keV range, and the best-fit parameters to be discordant with those measured by EPIC/XMM in a slightly higher energy band.



where  $p$  is detected C-band flux, and  $q$  is the C-band model prediction according to the thermal models of Table 3. A value of, e.g.,  $\eta=0.2$  in the fractional excess plots indicates that C-band emission is detected at the level of 20% excess with respect to the hot ICM emission at that cluster position. The effects of any gradients in the temperature (e.g., De Grandi and Molendi 2002) and abundance (e.g., De Grandi and Molendi 2001) distribution with cluster radius on the soft excess fluxes is accounted for by the spatially resolved modeling of the hot ICM. Uncertainties in the hot ICM parameters are also considered. The total errors  $\Delta\eta$  are in fact obtained by proper addition of statistical uncertainties in C-band fluxes ( $\Delta p$ ) and statistical uncertainties in the hot ICM models ( $\Delta q$ ). The latter is calculated as the sum of model variations when the best-fit  $T$  is varied by  $\Delta T = \pm 10\% T$  ( $\Delta q_T$ ) and the best-fit  $A$  by  $\Delta A = \pm 30\% A$  ( $\Delta q_A$ ); this choice is consistent with the published hot ICM model uncertainties for the clusters in this sample (see Table 3 for references), and it is oftentimes a conservative estimate (e.g., as in the cases of Coma or Virgo, where temperatures are known with accuracy of  $\sim 1 - 2\%$ ). This method of estimation of hot ICM model uncertainties is therefore uniform throughout the sample, and does not depend on the quality of the PSPC data or of the other data used to determine the best-fit ICM models.

Table 2—Continued

Cluster	Obs. ID	Obs. date	Exp. time (ks)
A2670	800420	29/6/92	14.7
A2717	800347	23/5/93	8.8
A2744	800343	16/6/92	13.6
A3301	800391	22/9/92	8.3
A3558	800076	17/7/91	28.0
A3560	800381	9/8/92	5.3
A3562	800237	19/1/93	17.6
A3571	800287	12/8/92	5.1
A4059	800175	21/1/91	5.3
Coma (A1656)	800005	17/6/91	20.8
Fornax (AS373)	600043	15/8/91	52.8
Hercules (A2151)	800517	17/8/93	11.0
Virgo	800187	10/6/92	9.4

Table 3. Spatially resolved best-fit models of the hot ICM and C-band fluxes for all clusters.

Region (arcmin)	kT (keV)	A	$\chi_r^2$	C-band flux $10^{-2} \text{c s}^{-1}$	$L_{NT}$ $10^{41} \text{ erg s}^{-1}$	$L_{therm}$ $10^{41} \text{ erg s}^{-1}$
<b>A21</b> ( $z=0.055$ , $N_H = 3.7$ , Ref: [E96])						
0-1	4	0.4	0.71(22)	$0.57 \pm 0.1$ (0.58)	...	...
1-3	$4 \pm_{1.6}^{5.5}$	0.3	0.88(47)	$1.25 \pm 0.16$ (1.33)	...	...
3-6	$6.5 \pm_{3.7}$	0.3	1.17(51)	$1.2 \pm 0.26$ (1.1)	...	...
6-9	5	0.3	0.71(39)	$1 \pm 0.33$ (0.51) (16%)	...	...
9-12	5	0.3	0.95(38)	$0.16 \pm 0.2$ (0.19) (2%)	...	...
<b>A85</b> ( $z=0.055$ , $N_H=2.7$ , Ref:[W00,L01,MFSV98])						
0-1	$3.4 \pm_{0.7}^1$	0.5	1.12(130)	$9.8 \pm 0.35$ (10.68)	...	...
1-3	$5.1 \pm_{1.2}^{1.9}$	0.5	1.09(139)	$14.6 \pm 0.43$ (13.47)	$2.3 \pm_{2.3}^{85}$	$6.5 \pm_{6.5}^5$
3-6	7	0.3	1.13(138)	$12.0 \pm 0.35$ (11.7)	...	...
6-9	7	0.3	0.89(123)	$7.6 \pm 0.28$ (6.5)	$9.1 \pm_{9.1}^{15}$	$3.8 \pm_{3.8}^5$
9-12	7	0.3	0.91(101)	$4.7 \pm 0.26$ (4.1)	$1.3 \pm_{1.3}^{15}$	$1.4 \pm_{1.4}^6$
12-15	7	0.3	0.99(73)	$2.1 \pm 0.3$ (2.2) (15%)	...	...
<b>A133</b> ( $z=0.057$ , $N_H=1.5$ , Ref:[R81,I02])						
0-1	$2.6 \pm_{0.4}^{0.4}$	$1.6 \pm_{0.5}^{1.5}$	1.24(119)	$8.2 \pm 0.23$ (6.5)	$14 \pm 0.4$	$7.5 \pm_{2.2}^{2.4}$
1-3	$4.1 \pm_{1.6}^{1.6}$	$0.44 \pm_{0.37}^{0.72}$	0.88(123)	$8.8 \pm 0.25$ (7.9)	$8.2 \pm_{6.5}^8$	$3.2 \pm_{2.1}$
3-6	$5.7 \pm_{2}^{5.5}$	0.3	1.11(111)	$6.6 \pm 0.26$ (5.3)	$4.6 \pm_{4.6}^{8.5}$	$6.5 \pm_{2.1}^{2.3}$
6-9	5	0.3	0.91(77)	$2.6 \pm 0.24$ (2.4)	...	...
9-12	5	0.3	1.09 (56)	$1 \pm 0.25$ (1.17) (11%)	...	...
<b>A665</b> ( $z=0.186$ , $N_H=4.3$ , Ref:[W00])						
0-1	$5 \pm_{1.1}^{1.8}$	0.3	1.14(122)	$9.6 \pm 0.58$ (11.6)	...	...
1-3	7	0.3	0.86(131)	$1.43 \pm 0.09$ (1.41)	...	...
3-6	7	0.3	1.02 (126)	$0.8 \pm 0.13$ (0.91) (16%)	...	...
<b>A1045</b> ( $z=0.138$ , $N_H=1.4$ )						
0-1	$3.8 \pm_{1.5}^{3.7}$	0.3	0.86(43)	$2.7 \pm 0.18$ (3.3)	...	...
1-3	$4.5 \pm_{2.1}$	0.3	0.7(28)	$1.86 \pm 0.21$ (1.89)	...	...
3-6	$8.8 \pm_{6.3}$	0.3	0.36(20)	$0.43 \pm 0.32$ (0.78) (6%)	...	...
<b>A1068</b> ( $z=0.139$ , $N_H=1.57$ , Ref:[W00])						
0-1	$3.3 \pm_{0.9}^{1.6}$	0.3	1.28(90)	$8.4 \pm 0.3$ (8.6)	...	...
1-3	5	0.3	0.71(45)	$34 \pm 0.23$ (27.5)	$55 \pm 34$	$24 \pm 13$
3-6	5	0.3	1.02(24)	$0.6 \pm 0.28$ (1) (10%)	...	...
<b>A1302</b> ( $z=0.116$ , $N_H=1.0$ , Ref:[E96])						

Table 3—Continued

Region (arcmin)	kT (keV)	A	$\chi_r^2$	C-band flux $10^{-2} \text{c s}^{-1}$	$L_{NT}$ $10^{41} \text{ erg s}^{-1}$	$L_{therm}$ $10^{41} \text{ erg s}^{-1}$
0-1	4.8	0.3	1.33(8)	2.63±0.35 (2.83)	...	...
1-3	4.8	0.3	0.99(10)	4±0.5 (3.4)	9.3± $^{38.5}_{9.3}$	3.1± $^{12}_{2.8}$
3-6	4.8	0.3	0.30(7)	2.4±0.62 (1.8)	...	...
6-9	2.4± $_{1.4}$	0.3	0.31(3)	0.8±0.7 (0.9) (10%)	...	...
<b>A1314</b> ( $z=0.034$ , $N_H=1.6$ , Ref:[E96])						
0-6	5± $_{3.2}$	0.3	0.71(15)	5.33±0.8 (3.7)	5.6± $^{6.9}_{5.6}$	2.5± $^{2.3}_{2.5}$
6-9	5	0.3	0.72(13)	3.5±0.9 (1.77)	6.2± $^{7.8}_{6.2}$	2.8± $^{4.2}_{2.8}$
9-12	5	0.3	0.57(10)	0.3±0.9 (1.4) (3%)	...	...
<b>A1361</b> ( $z=0.116$ , $N_H=2.5$ , Ref:[E96])						
0-1	2.2± $^{1.4}_{0.5}$	0.54± $^2_{0.4}$	0.86(27)	2.44±0.26 (2.82)	...	...
1-3	2.9± $^{7.1}_{1.2}$	0.3	0.67(14)	1.77±0.28 (1.5)	...	...
3-6	5	0.3	1.4(8)	0.64±0.4 (0.5) (14%)	...	...
<b>A1367</b> ( $z=0.0277$ , $N_H=1.7$ , Ref:[I02])						
0-3	3.4± $^{2.2}_{1.2}$	0.3	1.39(113)	4.8±0.19 (4.83)	...	...
3-6	2.5± $^{0.5}_{0.35}$	0.3	0.99(134)	10.3±0.3 (10.17)	...	...
6-9	3.6 ± $^{1.1}_{0.7}$	0.3	0.94(136)	10.26± 0.33 (10.07)	...	...
9-12	3.2	0.3	0.98(137)	9.8±0.36 (9.4)	...	...
12-15	3.2	0.3	1.06(134)	7.85±0.37 (7.96) (37%)	...	...
<b>A1413</b> ( $z=0.143$ , $N_H=1.71$ , Ref:[W00])						
0-1	8	0.4	0.79(69)	5.4±0.28 (5.63)	...	...
1-3	6	0.3	1.07(72)	6.5±0.3 (5.85)	5± $^4_5$	16± $^{21}_{16}$
3-6	6	0.3	1.2(36)	2.39±0.31 (2.1)	...	...
6-9	6	0.3	0.84 (22)	0.26±0.33 (0.69)(3.5%)	...	...
<b>A1689</b> ( $z=0.181$ , $N_H=1.72$ , Ref:[W00])						
0-1	5.1± $^{1.31}_{1.1}$	0.5	1.25(124)	8.46±0.25 (9)	...	...
1-3	8	0.3	1.04(107)	5.27±0.226 (5)	0.7± $^{16}_{0.7}$	8.6± $^{27}_{8.6}$
3-6	7	0.3	0.85(52)	1.57±0.23 (1.54) (23%)	...	...
<b>A1795</b> ( $z=0.063$ , $N_H=10.1$ , Ref:[BH96])						
0-1	3.6± $^{0.3}_{0.2}$	0.73± $^{0.15}_{0.12}$	1.04(301)	35.0±0.28 (32.83)	17±5.3	7±1.6
1-2	6.4± $^1_{0.8}$	0.58± $^{0.42}_{0.37}$	1.14(300)	23.9±0.24 (20.22)	34± $^{4.5}_{2.8}$	15±1.4
2-3	6.2± $^{1.3}_{1}$	0.56± $^{0.66}_{0.42}$	1.27(287)	14.1±0.19 (12.2)	17±2.9	7.3±1.1
3-6	7	0.3	1.13(290)	21.7±0.22 (19.53)	19±4.6	8.3± $^{1.6}_{1.4}$

Table 3—Continued

Region (arcmin)	kT (keV)	A	$\chi_r^2$	C-band flux $10^{-2} \text{c s}^{-1}$	$L_{NT}$ $10^{41} \text{ erg s}^{-1}$	$L_{therm}$ $10^{41} \text{ erg s}^{-1}$
6-9	7	0.3	0.97(278)	$8.05 \pm 0.15$ (7.5)	$3.2 \pm_{3.2}^{3.4}$	$1.7 \pm_{1.4}^{1.5}$
9-12	7	0.3	0.85(244)	$3.44 \pm 0.15$ (3.45) (19%)	...	...
<b>A1914</b> ( $z=0.171$ , $N_H=0.95$ , Ref:[W00])						
0-1	10	0.5	1.21(82)	$11.05 \pm 0.42$ (11.1)	...	...
1-3	10	0.3	0.98(58)	$8.4 \pm 0.4$ (7.7)	$4.7 \pm_{4.7}^{56}$	$5.7 \pm_{5.7}^{22}$
3-6	9	0.3	1(151)	$2.2 \pm 0.37$ (2.33) (25%)	...	...
6-9	8	0.3	0.7(22)	$0 \pm 0.71$ (0.6) (0%)	...	...
<b>A1991</b> ( $z=0.058$ , $N_H=2.25$ , Ref:[E96])						
0-3	$2.0 \pm_{0.18}^{0.2}$	$0.78 \pm_{0.19}^{0.25}$	1.1(136)	$6.5 \pm 0.2$ (7.16)	...	...
3-6	$3.5 \pm_{1.15}^{2.7}$	$0.65 \pm_{0.58}^{3.3}$	0.81(88)	$1.89 \pm 0.18$ (1.59)	$0.53 \pm_{0.53}^{19}$	$2 \pm_2^{6.3}$
6-9	4	0.3	0.89(70)	$0.78 \pm 0.2$ (0.51) (10%)	...	...
<b>A2029</b> ( $z=0.077$ , $N_H=3.2$ , Ref:[MFSV98])						
0-1	$3.5 \pm_{0.4}^{0.8}$	0.5	1.04(144)	$13.23 \pm 0.37$ (13.9)	...	...
1-3	9	0.3	1.07(145)	$13.36 \pm 0.387$ (11.98)	$21 \pm_{21}^{41}$	$22 \pm_{13}^{15.5}$
3-6	9	0.3	0.95(134)	$6.86 \pm 0.34$ (6.24)	$1.6 \pm_{1.6}^{34}$	$11 \pm_{11}^{13.5}$
6-9	9	0.3	1.05(107)	$2.81 \pm 0.33$ (2.72)	...	...
9-12	9	0.3	0.85(82)	$0.09 \pm 0.35$ (1.34) (8.2%)	...	...
<b>A2142</b> ( $z=0.09$ , $N_H=4.15$ , Ref:[HB96])						
0-1	$5.8 \pm_{1.2}^{1.85}$	$0.67 \pm_{0.6}^{1.1}$	0.89(149)	$5.69 \pm 0.2$ (5.66)	...	...
1-3	9	0.3	0.75(151)	$7.93 \pm 0.2$ (7.72)	...	...
3-6	9	0.3	0.90(144)	$5.26 \pm 0.24$ (4.87)	$1.6 \pm_{1.6}^{37}$	$12 \pm_{12}^{19.6}$
6-9	9	0.3	0.69(136)	$2.16 \pm 0.24$ (2.6)	...	...
9-12	9	0.3	0.68(104)	$0.94 \pm 0.35$ (1)	...	...
12-15	9	0.3	0.60(92)	$0.59 \pm 0.25$ (0.65)	...	...
<b>A2199</b> ( $z=0.03$ , $N_H=0.85$ , Ref:[MVFS99,SSJ98])						
0-1	$3.2 \pm 0.7$	0.4	1.19(138)	$28.2 \pm 0.54$ (33.27)	...	...
1-2	$4.3 \pm_{0.9}^{1.4}$	0.4	0.93(137)	$32.14 \pm 0.58$ (30.53)	$0.05 \pm_{0.05}^{0.96}$	$0.46 \pm_{0.46}^{0.7}$
2-3	$4.2 \pm_{1.1}^{1.7}$	0.3	1.09(129)	$22.61 \pm 0.5$ (23.72)	...	...
3-6	4.5	0.3	1.05(146)	$46.94 \pm 0.76$ (47.37)	...	...
6-9	4.5	0.3	0.92(130)	$24.53 \pm 0.63$ (23.6)	$0.5 \pm 0.5$	$0.22 \pm_{0.22}^{0.4}$
9-12	4.5	0.3	1.03(114)	$12.55 \pm 0.57$ (12.69)	...	...
12-15	4.5	0.3	0.95(90)	$8.98 \pm 0.59$ (7.18)	$4.8 \pm_{3.4}^{3.3}$	$1.7 \pm_{1.15}^{1.1}$

Table 3—Continued

Region (arcmin)	kT (keV)	A	$\chi_r^2$	C-band flux $10^{-2} \text{c s}^{-1}$	$L_{NT}$ $10^{41} \text{ erg s}^{-1}$	$L_{therm}$ $10^{41} \text{ erg s}^{-1}$
15-18	4.5	0.3	0.65(81)	$5.9 \pm 0.62$ (5.2) (19%)	...	...
<b>A2218</b> ( $z=0.17$ , $N_H=2.75$ , Ref:[W00,NB99])						
0-1	$5.4 \pm_{1.4}^{2.3}$	$0.36 \pm_{0.36}^{1.95}$	1.32(118)	$1.93 \pm 0.08$ (1.77)	$0.47 \pm_{0.47}^{61}$	$12 \pm_{12}^{15.3}$
1-3	7	0.2	1.17(124)	$2.35 \pm 0.1$ (1.93)	$59 \pm_{34.5}^{44}$	$29 \pm 19$
3-6	6	0.2	0.88(103)	$1.1 \pm 0.14$ (8.5) (16%)	...	...
6-9	5	0.2	1.37(78)	$0.05 \pm 0.17$ (0.28) (1%)	...	...
<b>A2219</b> ( $z=0.23$ , $N_H=2.04$ , Ref:[W00])						
0-1	$6.6 \pm_{2.6}^{10}$	0.3	0.97(61)	$3.6 \pm 0.21$ (3.7)	...	...
1-3	7	0.3	0.94(75)	$5 \pm 0.28$ (4.7)	$5.6 \pm_{5.6}^{75}$	$12 \pm_{12}^{34}$
3-6	7	0.3	0.99(46)	$2.51 \pm 0.32$ (2.2)	...	...
6-9	7	0.3	0.79(27)	$1 \pm 0.4$ (0.7) (12%)	...	...
<b>A2241</b> ( $z=0.063$ , $N_H=2.05$ , Ref:[WJF97])						
0-1	$2.1 \pm_{0.4}^{1.6}$	0.3	0.89(39)	$1.42 \pm 0.13$ (2.14)	...	...
1-3	3.1	0.3	0.83(27)	$0.92 \pm 0.16$ (1.17)	...	...
3-6	3.1	0.3	0.86(21)	$0.51 \pm 0.26$ (0.528) (10%)	...	...
<b>A2244</b> ( $z=0.097$ , $N_H=1.9$ , Ref:[WJF97])						
0-1	$3.4 \pm_{1.1}^{3.1}$	0.3	1.0(20)	$7.2 \pm 0.5$ (7.46)	...	...
1-3	$4 \pm_{1.5}^{4.9}$	0.3	0.79(56)	$8.3 \pm 0.57$ (7.8)	...	...
3-6	7	0.3	0.46(24)	$3.56 \pm 0.53$ (3.6)	...	...
6-9	7	0.3	2.4(14)	$1.14 \pm 0.55$ (1.39) (14%)	...	...
<b>A2255</b> ( $z=0.08$ , $N_H=2.51$ , Ref:[W00,I02])						
0-1	8	0.3	0.46(33)	$0.74 \pm 0.08$ (0.79)	...	...
1-3	7	0.3	1.29(106)	$3.8 \pm 0.18$ (3.38)	$21 \pm_{13}^{14}$	$5.3 \pm_5^6$
3-6	7	0.3	0.77(119)	$5.4 \pm 0.26$ (4.5)	$19 \pm_{15.5}^{17}$	$7 \pm_3^{3.2}$
6-9	7	0.3	0.84(99)	$2.77 \pm 0.26$ (2.59)	...	...
9-12	6	0.3	1.36(65)	$2.1 \pm 0.29$ (1.32) (19%)	...	...
12-15	5	0.3	0.84(54)	$1.18 \pm 0.31$ (0.8) (10%)	...	...
<b>A2256</b> ( $z=0.06$ , $N_H=4.55$ , Ref:[MSFV98,B91])						
0-3	7	0.3	1.05(147)	$5.5 \pm 0.197$ (5.28)	...	...
3-6	7	0.3	1.13(149)	$6.74 \pm 0.24$ (6.5)	...	...
6-9	7	0.3	1.29(140)	$3.64 \pm 0.22$ (3.3)	$1.2 \pm_{1.2}^{16}$	$4.2 \pm 4.2$
9-12	7	0.3	0.85(125)	$1.52 \pm 0.21$ (1.6) (22%)	...	...

Table 3—Continued

Region (arcmin)	kT (keV)	A	$\chi_r^2$	C-band flux $10^{-2} \text{c s}^{-1}$	$L_{NT}$ $10^{41} \text{ erg s}^{-1}$	$L_{therm}$ $10^{41} \text{ erg s}^{-1}$
<b>A2597</b> ( $z=0.085$ , $N_H=2.2$ , Ref:[W00,I02])						
0-1	$2.5 \pm_{0.6}^{0.4}$	0.3	1.12(140)	$13.1 \pm 0.44$ (12.92)	...	...
1-3	$4.3 \pm_{1.5}^{4.2}$	0.3	0.78(65)	$6.8 \pm 0.34$ (4.9)	$58 \pm_{24}^{29}$	$25 \pm 8.7$
3-6	4	0.3	1.07(35)	$1.84 \pm 0.3$ (1.93)	...	...
6-9	4	0.3	1.04(21)	$0.66 \pm 0.33$ (0.69)	...	...
<b>A2670</b> ( $z=0.076$ , $N_H=2.73$ , Ref: [W00,HW97])						
0-1	$3.2 \pm_{0.9}^{2.1}$	$1 \pm_{0.6}^{3.6}$	1.3(61)	$1.27 \pm 0.1$ (1.5)	...	...
1-3	3	0.3	1.11(98)	$2 \pm 0.15$ (2.85)	...	...
3-6	3	0.3	1.09(69)	$2 \pm 0.22$ (1.51)	$2.7 \pm_{2.7}^{11}$	$2.2 \pm 2.2$
6-9	3	0.3	1.42(46)	$0.63 \pm 0.26$ (0.68) (10%)	...	...
<b>A2717</b> ( $z=0.049$ , $N_H=1.23$ , Ref:[L97])						
0-1	$1.8 \pm_{0.25}^{0.4}$	0.5	1.25(35)	$2.81 \pm 0.18$ (2.8)	...	...
1-3	$1.8 \pm_{0.3}^{0.6}$	$0.19 \pm_{0.14}^{0.29}$	1.04(49)	$5.2 \pm 0.28$ (5.0)	...	...
3-6	$3.1 \pm_{1.2}^{4.1}$	0.3	0.83(44)	$3.3 \pm 0.32$ (3.3)	...	...
6-9	$2.7 \pm_{1.1}^7$	0.3	1.12(27)	$1.28 \pm 0.30$ (1.26)	...	...
<b>A2744</b> ( $z=0.31$ , $N_H=1.41$ , Ref:[E96,A00])						
0-1	11	0.2	1.17(50)	$2.52 \pm 0.14$ (2.21)	$48 \pm_{48}^{88}$	$36 \pm_{36}^{51}$
1-3	11	0.2	1.25(56)	$3.28 \pm 0.18$ (2.38)	$290 \pm 107$	$170 \pm 60$
3-6	11	0.2	0.77(36)	$1.54 \pm 0.23$ (0.92)	$160 \pm_{148}^{140}$	$110 \pm_{99}^{73}$
6-9	11	0.2	0.83(21)	$0.64 \pm 0.26$ (0.32) (9%)	...	...
<b>A3301</b> ( $z=0.054$ , $N_H=2.49$ )						
0-1	$1.7 \pm_{0.35}^1$	0.3	0.93(14)	$0.51 \pm 0.1$ (0.66)	...	...
1-3	$11 \pm_8$	0.3	0.9(34)	$1.54 \pm 0.2$ (1.38)	...	...
3-6	$7 \pm_4$	0.3	1.3(41)	$2 \pm 0.31$ (1.5)	$9.4 \pm_{8.5}^{10}$	$4.1 \pm_{4.1}^{4.5}$
6-9	$2.1 \pm_{0.6}$	0.3	0.77(35)	$0.57 \pm 0.42$ (0.95) (6%)	...	...
<b>A3558</b> ( $z=0.048$ , $N_H=4.0$ , Ref:[MFSV98])						
0-1	$2.8 \pm_{0.5}^{0.7}$	$0.48 \pm_{0.22}^{0.36}$	1.31(117)	$2.02 \pm 0.3$ (1.69)	...	...
1-3	$3.3 \pm_{0.5}^{0.6}$	$0.26 \pm_{0.15}^{0.16}$	1.08(142)	$4.45 \pm 0.14$ (4.18)	$0.76 \pm_{0.76}^{9.2}$	$2.8 \pm 2.8$
3-6	5	0.3	1.19(150)	$6.86 \pm 0.2$ (6)	$15 \pm_6^{11}$	$13 \pm_{4.5}^{5.5}$
6-9	5	0.3	1.15(146)	$5.1 \pm 0.23$ (3.9)	$28 \pm_7^9$	$19 \pm 6.3$
9-12	5	0.3	0.98(139)	$2.5 \pm 0.21$ (2.1) (22%)	...	...
<b>A3560</b> ( $z=0.04$ , $N_H=4.7$ , Ref:[W00])						

Table 3—Continued

Region (arcmin)	kT (keV)	A	$\chi_r^2$	C-band flux $10^{-2} \text{c s}^{-1}$	$L_{NT}$ $10^{41} \text{ erg s}^{-1}$	$L_{therm}$ $10^{41} \text{ erg s}^{-1}$
0-3	$2.1 \pm_{0.6}^{1.3}$	$0.27 \pm_{0.23}^{0.62}$	1.15(39)	$1.23 \pm 0.23$ (1.36)	...	...
3-6	$4.1 \pm_2$	0.3	1.25(45)	$1.98 \pm 0.34$ (1.29)	$0.8 \pm_{0.8}^{15}$	$3.6 \pm_{3.6}^{10.5}$
6-12	$2 \pm_{0.5}^{1.4}$	$0.4 \pm_{0.3}^{1.4}$	1.35 (54)	$2.1 \pm 0.6$ (1.4) (14%)	...	...
<b>A3562</b> ( $z=0.04$ , $N_H=4.01$ , Ref:[I02])						
0-1	$2.4 \pm_{0.4}^{0.8}$	0.6	1.01(130)	$1.12 \pm 0.088$ (1.05)	...	...
1-3	$2.7 \pm_{0.65}^{0.7}$	0.6	1.02(142)	$2.9 \pm 0.16$ (2.5)	$0.4 \pm_{0.4}^{3.8}$	$2.4 \pm_{2.4}^{3.5}$
3-6	$4.8 \pm_{0.75}^{2.3}$	0.4	0.82(131)	$3.38 \pm 0.23$ (2.7)	$5.2 \pm_{5.2}^{8.2}$	$4 \pm_4^{5.2}$
6-12	$3.6 \pm_{0.8}^{1.1}$	0.4	1.32(133)	$3.5 \pm 0.4$ (3.15) (15%)	...	...
<b>A3571</b> ( $z=0.04$ , $N_H=4.4$ , Ref:[MSFV98])						
0-2	$5.3 \pm_{1.7}^{5.2}$	0.5	0.81(118)	$9.03 \pm 0.42$ (7.3)	$1 \pm_1^9$	$2.6 \pm_{2.6}^{3.8}$
2-4	7	0.3	0.98(129)	$8.65 \pm 0.46$ (7.94)	$1.3 \pm_{1.3}^{8.3}$	$4.5 \pm_{4.5}^{6.7}$
4-6	7	0.3	1.24(112)	$6.7 \pm 0.45$ (5.9)	$1.3 \pm_{1.3}^{23}$	$13 \pm_{13}^{18}$
6-8	7	0.3	1.29(76)	$3.9 \pm 0.38$ (2.9)	$0.7 \pm_{0.7}^{20.5}$	$7.4 \pm_{7.4}^{11}$
8-12	7	0.3	0.92(94)	$4.2 \pm 0.54$ (3.27)	$0.25 \pm_{0.25}^{5.2}$	$3.4 \pm_{3.4}^{15}$
12-16	5	0.3	1.21(88)	$2.7 \pm 0.62$ (1.93) (16%)	...	...
<b>A4059</b> ( $z=0.046$ , $N_H=1.06$ , Ref: [MFSV98])						
0-1	$2.3 \pm_{0.4}^{0.9}$	0.5	1.39(64)	$9 \pm 0.41$ (10.46)	...	...
1-3	$3.9 \pm_{1.2}^2$	$0.7 \pm_{0.5}^{1.5}$	0.86(95)	$16.56 \pm 0.58$ (15.16)	...	...
3-6	5	0.3	0.71(78)	$11.2 \pm 0.56$ (11.64)	...	...
6-9	4	0.3	0.97(46)	$4.9 \pm 0.5$ (5.9)	...	...
9-12	4	0.3	1.05(31)	$0.25 \pm 0.52$ (0.28) (19%)	...	...
<b>Coma (A1656)</b> ( $z=0.023$ , $N_H=0.9$ , Ref: [I02])						
0-3	8.2	0.2	1.19(150)	$44.5 \pm 0.48$ (36.37)	$11 \pm_{1.1}^1$	$4.6 \pm_{0.3}^{0.56}$
3-6	8.2	0.2	1.23(150)	$92.9 \pm 0.7$ (76.9)	$22 \pm 1.6$	$9.1 \pm 0.7$
6-9	8.2	0.2	1.56(150)	$99.1 \pm 0.75$ (81.1)	$26 \pm 1.4$	$10 \pm_{1.1}^{0.86}$
9-12	8.2	0.2	1.12(150)	$84.8 \pm 0.73$ (67.8)	$25 \pm_{2}^{1.7}$	$10 \pm_{0.5}^{0.7}$
12-18	8.2	0.2	1.2 (150)	$123 \pm 1$ (90.7)	$47 \pm_{2.7}^{2.3}$	$21 \pm_{0.5}^{0.9}$
<b>Fornax (AS373)</b> ( $z=0.0064$ , $N_H=1.5$ , Ref:[J97])						
0-1	$0.91 \pm_{0.02}^{0.03}$	$0.47 \pm_{0.05}^{0.07}$	1.37(148)	$3.16 \pm 0.08$ (3.7)	...	...
1-2	$1.28 \pm_{0.07}^{0.04}$	$0.89 \pm_{0.2}^{0.37}$	1.23(149)	$2 \pm 0.073$ (1.4)	$0.026 \pm_{0.006}^{0.004}$	$0.021 \pm_{0.004}^{0.005}$
2-3	$1.38 \pm_{0.04}^{0.04}$	$1.18 \pm_{0.18}^{0.7}$	0.99(149)	$1.7 \pm 0.07$ (1.17)	$0.016 \pm_{0.004}^{0.008}$	$0.017 \pm_{0.004}^{0.0035}$
3-6	$1.57 \pm_{0.09}^{0.09}$	$0.98 \pm_{0.18}^{0.28}$	0.77(140)	$5.7 \pm 0.15$ (4.4)	$0.053 \pm_{0.016}^{0.01}$	$0.034 \pm 0.007$



## 4. Results

Results of the spatially resolved C-band emission of all clusters are reported in Table 3, and the average fractional excesses  $\eta$  for all clusters are summarized in Fig. 1. Statistically significant detection of soft excess emission throughout the whole cluster was achieved for A85, A133, A1314, A1795, A2218, A2597, A2744, A3558, A3562, A3571, Coma, Fornax and Virgo. In particular, large statistical significance is displayed by those sources with the deepest observations (Coma, Virgo, Fornax, A3558, A1795). On the other hand, our available PSPC data appear to rule out excess emission throughout the entire cluster extent only in a few sources (A1045, A665, A2241). The distribution of the soft excess emission/absorption with cluster radius varies within the sample, and it is shown in detail for each cluster in Fig. 2. The large number of clusters analyzed in this paper (38) warrants however an investigation of the general properties of the sample as a whole. The distribution of the soft excess emission is spatially unresolved, at the resolution of PSPC, in most clusters where excess is found with large statistical significance (e.g., A1795, Fornax, Coma, Virgo, A2744); in only two cases the soft excess emission seems to be localized (A85 and A2256, see section 6 for details). We therefore focus on the soft X-ray properties of the azimuthally averaged annuli of all clusters.

Clusters span an interval of redshifts from  $z=0.0043$  (Virgo) to  $z=0.308$  (A2744); we accordingly plotted the composite distribution of the C-band fractional excesses  $\eta$  of all cluster regions as function of physical distance from the cluster center (in Mpc, Fig. 3; a Hubble constant of  $H_0 = 75 \text{ km s}^{-1} \text{ Mpc}^{-1}$  is assumed hereafter). Only regions for which C-band signals exceed 25% of the background are analyzed, and each region is reported in the following plots (Figs. 3,5,6,7 and 8) as a data point at its mean radius; horizontal error bars are omitted for clarity. When all radii are considered, we found that 91 datapoint-regions lay above the 0% excess line, and 38 below it. A closer look at Fig. 3 however reveals that, although amidst large statistical uncertainties, a break point in the distribution occurs in the 150-200 kpc region. For radii  $\leq 170$  kpc, the distribution reveals a large scatter, and no evidence of a bias towards positive  $\eta$ . Quantitatively, 36 points lay above the no-excess line, and 27 below it. For radii larger than 170 kpc, all regions (with the exception of one) are either statistically consistent with no excess, or significantly in excess. In numbers, 55 points exceed  $\eta = 0$ , and 11 have  $\eta < 0$ . Fig. 4 summarizes this behavior, whereby the average soft excess for all cluster regions is  $\sim 9\%$  (Fig. 4, top). Central cluster regions, however, have negligible net average soft excess emission (Fig. 4, center), while outer cluster regions have an average soft excess of 13% (Fig. 4, bottom). A similar result is borne out by Fig. 5, where all data points are plotted as function of their respective X-ray core radii (see Table 1). The breakpoint is now located at  $\sim 0.5\text{-}0.6$  core radii; above it, the large majority of data points represent excess emission.

Table 3—Continued

Region (arcmin)	kT (keV)	A	$\chi_r^2$	C-band flux $10^{-2} \text{C s}^{-1}$	$L_{NT}$ $10^{41} \text{ erg s}^{-1}$	$L_{therm}$ $10^{41} \text{ erg s}^{-1}$
6-9	$1.51 \pm_{0.09}^{0.1}$	$0.61 \pm_{0.13}^{0.15}$	0.92(142)	$5.7 \pm 0.18$ (5.0)	$0.027 \pm 0.0016$	$0.018 \pm 0.01$
9-12	$1.5 \pm_{0.07}^{0.08}$	$0.73 \pm_{0.16}^{0.17}$	1.35(142)	$4.97 \pm 0.2$ (4.92)	...	...
12-15	$1.4 \pm_{0.03}^{0.03}$	$0.87 \pm_{0.19}^{0.13}$	0.94(142)	$0.47 \pm 0.23$ (0.465) (23%)	...	...
15-18	$1.35 \pm_{0.04}^{0.04}$	$0.71 \pm_{0.16}^{0.17}$	0.90(143)	$0.42 \pm 0.25$ (0.51) (18%)	...	...
<b>Hercules (A2151)</b> ( $z=0.037$ , $N_H=3.2$ , Ref:[HS96])						
0-1 L	$1.7 \pm_{0.19}^{0.24}$	0.5	0.96(53)	$1.48 \pm 0.12$ (1.5)	...	...
1-3 L	$2.4 \pm_{0.5}^{0.9}$	$0.7 \pm_{0.35}^{0.8}$	0.99(81)	$3.1 \pm 0.2$ (2.33)	...	...
0-1 R	$1.2 \pm_{0.2}^{0.2}$	$0.24 \pm 0.7_{0.2}$	0.92(12)	$0.35 \pm 0.073$ (0.35)	...	...
1-3 R	$1.28 \pm_{0.14}^{0.32}$	$0.16 \pm_{0.08}^{0.16}$	1.02(40)	$0.836 \pm 0.15$ (0.82)	...	...
<b>Virgo</b> ( $z=0.0043$ , $N_H=1.8$ )						
0-3	$1.77 \pm_{0.03}^{0.03}$	$1.14 \pm 0.1$	1.16(149)	$132 \pm 1.2$ (95.6)	$1.8 \pm 0.2$	$1.2 \pm 0.075$
3-6	$2.42 \pm_{0.16}^{0.29}$	$1.06 \pm_{0.15}^{0.17}$	1.1(149)	$110.7 \pm 1.1$ (83.6)	$1.6 \pm 0.14$	$0.9 \pm 0.08$
6-9	$2.9 \pm_{0.2}^{0.4}$	$0.88 \pm_{0.16}^{0.2}$	0.94(149)	$98.35 \pm 1.1$ (72.2)	$1.8 \pm_{0.16}^{0.14}$	$0.93 \pm 0.08$
9-12	$3.6 \pm_{0.4}^{0.7}$	$0.79 \pm_{0.2}^{0.21}$	1.24(149)	$76 \pm 1$ (56)	$1.5 \pm_{0.15}^{0.17}$	$0.7 \pm_{0.06}^{0.05}$
12-15	$3.0 \pm_{0.34}^{0.5}$	$0.59 \pm_{0.16}^{0.19}$	1.0(147)	$62.3 \pm 1$ (47.5)	$1.2 \pm_{0.15}^{0.17}$	$0.54 \pm_{0.07}^{0.06}$
15-18	$3.9 \pm_{0.7}^1$	$1.0 \pm_{0.3}^{0.75}$	1.17(149)	$43.2 \pm 1$ (32.9)	$0.82 \pm_{0.12}^{0.11}$	$0.41 \pm_{0.04}^{0.06}$

Note. — C-band fluxes are shown with their  $1-\sigma$  statistical uncertainties; in parentheses, the C-band percent flux above background for outermost cluster regions, where no percentage is shown C-band flux exceeds 25% of C-band background. kT and A errors are 90 % confidence intervals, where no errors are reported, the parameter was fixed and literature reference for T and A of each cluster is reported.  $L_{NT}$  is un-absorbed luminosity in 0.2-0.4 keV band of the excess emission, when modeled with a power-law model of photon index  $\alpha = 1.75$ , errors are 90% confidence on 2 free parameters (power-law normalizations constant and normalization constant of hot ICM MEKAL model).  $L_{therm}$  is un-absorbed luminosity in 0.2-0.4 keV band of the excess emission, when modeled with a second MEKAL model of KT=80 eV, A=0.3, errors are 90% confidence on 1 free parameter (normalization of second MEKAL model). Model luminosities have been redshift corrected (K correction),  $H_0=75 \text{ km s}^{-1} \text{ Mpc}^{-1}$ .

References:

E96 - Ebeling et al. 96; W00 - White 2000; L01 - Lima-Neto, Pislar and Bagchi 2001 (A85); R81 - Reichert et al. 1981 (A133); BH96 - Briel and Henry 1996 (A1795); MFSV98 - Markevitch, Forman, Sarazin and Vikhlinin 1998; HB96 - Henry and Briel 1996 (A2142); MVFS99 - Markevitch et al 1999 (A2199); SSJ98 - Siddiqui et al. 1998 (A2199); NB99 - Neumann and Bohringer 1999 (A2218); WJF97 - White, Jones and Forman 1997; B91 - Briel et al. 1991 (A2256); HW97 - Hobbs and Willmore 1997 (A2670); L97 - Liang et al. 1997 (A2717); A00 - Allen 2000; HS96 - Huang and Sarazin 1996 (Hercules); J97 - Jones et al. 1997 (Fornax); I02 - Ikebe et al. 2002.

We also offer an at-a-glance summary of the  $\eta$  distribution as function of detector radius in Fig. 6, primarily for the investigation of any possible systematic detector effects. The excess emission is confined to detector radii  $\geq 2$  arcmin and, to within the sparse sampling of our ensemble, rather uniformly distributed across the 2-18 arcmin region. It is also evident, from the individual plots of Fig. 2, that soft excess regions are detected at different detector positions and with different radial trends for different clusters, e.g., A1795, A2744, Coma or A1367<sup>3</sup>. It is therefore possible to rule out the possibility of detector non-uniformities and systematic miscalibrations as the cause of excess C-band counts. It is also possible to investigate any correlation of soft excess emission with  $N_H$ , given that our sample spans the  $0.8\text{--}5 \times 10^{20} \text{ cm}^{-2}$  range. Fig. 7 shows no evidence of a correlation of positive  $\eta$  regions with  $N_H$ . Obviously, at low  $N_H$ , many of the detections have larger statistical significance, as more photons penetrate the Galaxy. However, if the cross-sections for Galactic absorption were systematically off, we would expect a larger fraction of positive  $\eta$  regions at one end and a smaller fraction at the opposite end of the  $\eta$ - $N_H$  plot. Neither feature is however present in Fig. 7, indicating that cross-section errors are unlikely the cause of the C-band excess counts.

In Fig. 8 we also plot the composite  $\eta$  distribution of peripheral cluster regions where the C-band emission drops below 25% of the PSPC background (the dotted diamonds of Fig. 2), and therefore the most sensitive to background subtraction. All data points are consistent with no excess, indicating that the employed background subtraction method does not give rise to systematic under- or over-subtraction of signal.

We summarize the general properties of the C-band emission from this sample of galaxy clusters in the following points:

1. The excess emission co-exists (in a sample sense) with intrinsic excess absorption in the central regions of clusters (radii  $\leq 150\text{--}200$  kpc). This is indicated by the large scatter of the high signal-to-noise data points in this radial interval, with a mean value that is approximately consistent with  $\eta=0$ . Central soft X-ray absorption is detected with  $S/N \geq 3$  in  $\sim 20\%$  of the sources (A665, A2199, A2241, A2670, A4059, Fornax, A1991, see Fig. 2)
2. The soft excess is clearly present outside the central 0.5-0.6 X-ray core radii, or, alternatively, at radii  $\geq 170$  kpc. This therefore implies that, when the distribution at all physical radii is considered, excess emission is preferentially found in the outer regions.
3. The soft excess phenomenon is widespread. Not only  $\eta > 0$  regions are the typical feature of Figs. 1 through 7, but excess is detected with large statistical significance (e.g.,  $S/N \geq 3\text{--}4$ ) preferentially in the deepest observations, as expected of any genuine celestial phenomenon

---

<sup>3</sup>All of these observations share the same boresight position in PSPC detector coordinates.

(see A1795, A85, Coma, Virgo, Fornax, A3571 and A3558; A2199 is the only cluster for which a deep PSPC observation did not reveal soft excess with large S/N).

4. The soft excess emission seldom exceeds 40-50% of the hot ICM contribution. It is evident that clusters like Sérsic 159-03 (Bonamente, Lieu and Mittaz 2001d), where the soft excess reaches a prominence of 50-100% in PSPC C-band, are exceptional. Few cases where comparison with *EUVE*/DS data in the  $\sim 65$ -190 eV band is available (Coma, Virgo, A2199, A1795; Lieu et al. 1996a,1996b; Mittaz, Lieu and Lockman 1998; Lieu, Bonamente and Mittaz 1999) suggest that the soft excess phenomenon may be intrinsically very *soft*, e.g. more suitably revealed with large  $\eta$  in the extreme-ultraviolet band.

## 5. Interpretation

The analysis reveals that the customary one-temperature hot ICM model fails to describe accurately the C-band emission of many clusters in this sample. Positive and negative residuals  $\eta$  are present in the majority of sources, and constitute a common trait in the composite plots of the whole sample. Central cluster regions (i.e.,  $\leq 150$ -200 kpc from the center) show evidence of intrinsic absorption in a fraction of the sources, and of excess emission in others (e.g., A133, Coma and Virgo). For radii  $\geq 200$  kpc, the 1-T model typically falls short of the detected emission, revealing the soft excess emission.

### (a) *C-band central absorption*

Intrinsic C-band absorption can be attributed to cold ( $T \leq 10^4$ K) gas in the center of galaxy clusters. There the hot ICM has radiative cooling times which are often significantly shorter than the cluster's age, and the hot gas is expected to cool to low temperatures (Fabian 1988). There is also evidence, from PSPC image analysis (Bonamente, Lieu and Mittaz 2001a), that cold absorbing gas may co-exists with the hot gas even in the absence of the excess absorption signature. Presence of cold, absorbing gas could then be responsible for excess C-band absorption in some clusters, and for the lack or lesser C-band excess emission in other clusters where the excess is evident at larger radii (e.g., A1795, Fornax etc.).

### (b) *Thermal and non-thermal modeling of the excess emission*

The nature of the excess component has been studied in detail for those sources for which the data quality allows a detailed modeling. The excess emission of Coma (Lieu et al. 1996b), Virgo (Lieu et al. 1996a; Bonamente, Lieu and Mittaz 2001b), A2199 (Lieu, Bonamente and Mittaz 1999), A1795 (Bonamente, Lieu and Mittaz 2001b), A3558 and A3571 (Bonamente et al. 2001c; and of Sérsic 159-03; Bonamente, Lieu and Mittaz 2001d, not included in this sample) indicate that the emission may be due to either a second phase of the ICM at lower temperature ( $T \sim 10^6$  K, the thermal 'warm' gas scenario), or to an Inverse-Compton

emission of cluster relativistic electrons that scatter microwave background photons (MWB, non-thermal model). Here we model the excess emission of those cluster regions where excess emission is detected with  $S/N \geq 1 \sigma$ , in order to provide estimates/upper limits to the soft X-ray luminosity of the excess component ( $L_{NT}$  and  $L_{therm}$  in Tables 3, 5, 6 and 7). Employed emission models are:

1. an optically thin plasma emission code (MEKAL) of  $kT=80$  eV and  $A=0.3$  solar (thermal model);

2. a power-law with photon index  $\alpha = 1.75$  (non-thermal model). This emission model is suggestive of Inverse Compton emission due to scattering of MWB photons with a population of relativistic electrons with differential number distribution  $n(E) \propto E^{-p}$ ,  $p=2.5$  (e.g., Lieu et al. 1999).

The two models indicate that the soft excess emission has a 0.2-0.4 keV luminosity which ranges between  $10^{40}$  erg  $s^{-1}$  and  $10^{43}$  erg  $s^{-1}$ , the latter figure applies to the strong soft excesses of Coma and A2744. In summary, either model successfully explains the data, but faces serious theoretical challenges. Sub-megakelvin gases cool radiatively in a short time by free-free and line emission. Our estimates require a warm gas density of  $\sim 10^{-3}$   $cm^{-3}$  or more (if the gas is substantially clumped) and  $T \sim 10^6$  K in order to explain typical soft excess fluxes (Bonamente, Lieu and Mittaz 2001b,2001d). The free-free cooling time of such gas,

$$t_{cool} \simeq 6 \times 10^9 \left(\frac{T}{10^6 K}\right)^{\frac{1}{2}} \left(\frac{n}{10^{-3} cm^{-3}}\right)^{-1} \text{ years} \quad (2)$$

is by itself already shorter than the Hubble time, and line cooling for metal abundances of  $A \sim 0.3$  solar further reduces the cooling time by a factor of about 5, or even more if the gas is cooler than  $10^6$  K (Landini and Monsignori-Fossi, 1990). A mechanism of continuous injection/reheating would therefore be necessary to sustain the emission for cosmological periods of time, (e.g., Fabian 1997) as its frequent occurrence is unlikely to be explained as a transitory phenomenon. On the other hand, the non-thermal model requires large amounts of cosmic-ray electrons, which may surpass the energy content of the hot phase (see, e.g., Bonamente, Lieu and Mittaz 2001d).

In order to obtain more precise estimates of the ‘warm’ gas masses and the non-thermal electron pressure implied by the soft excess it is necessary to know the precise temperature of the putative ‘warm’ gas, or alternatively the slope of the non-thermal power-law that best fits the soft excess. This information is unavailable for most of the clusters analyzed here, due to limited  $S/N$ . The case of Sérsic 159-03, where the fractional excess reaches  $\eta = 0.5 - 1$  in PSPC C-band (Bonamente, Lieu and Mittaz 2001d), can however be used as an upper limit for all clusters investigated in this sample. Its soft excess, when modeled as thermal emission, implied that an excess of  $\sim 40 - 50\%$  by mass (with respect to calculated hot ICM masses) resides as a warm phase of the ICM. Alternatively, relativistic electrons are

present in the ICM above pressure equipartition with the hot ICM by a factor of few. After a downward revision to match the present  $\eta \sim 0.1 - 0.5$  fractional excesses of this sample, the two scenarios imply that in a large fraction of galaxy clusters ( $\sim 50\%$ ) there is either an extra 10-40% of mass at sub-Virial temperatures, or a widespread population of relativistic electrons near pressure equipartition with the hot gas.

(c) *Radial distribution of the excess and non-thermal models*

Superior spectral resolving power is required to distinguish the signatures of ‘warm’ gas and of a non-thermal power-law from X-ray spectroscopy, marginally available even to the new generation X-ray instruments (XMM/EPIC and RGS, Chandra/LETG and ACIS). Alternatively, other wavelengths are also employed in the search of, e.g., thermal OVI lines from metal-rich sub-Virial gases in cluster, although yet unsuccessfully (e.g., Dixon et al. 2001); these results will be rendered obsolete if the putative warm gas is primordial. However, the soft excess radial distribution of clusters in this sample provides by itself additional clues toward understanding the nature of the phenomenon. The preferential distribution of soft excess emission at large cluster radii is naturally explained in the context of non-thermal Inverse Compton (IC) radiation. The distribution of the relativistic electrons as function of cluster radius  $r$  ( $n_e(r)$ ) may follow the gas distribution, while the MWB photons are uniformly distributed across the sky. With the hot ICM gas density distribution  $n(r)$  declining with radius, the hot ICM bremsstrahlung emission falls with radius like  $n^2(r)$ , while the IC emission only like  $n_e(r)=n(r)$ . Alternatively, if thermal and non thermal electrons coexist in an adiabatic environment, the different ratio of specific heats  $\gamma$  (5/3 for the hot ICM and 4/3 for the relativistic plasma) predicts a larger fraction of relativistic electrons at large cluster radii than at small radii with respect to the thermal gas, going further in the direction of explaining the presence of soft excess at large radii (e.g., Bonamente 2000). It is however possible, as discussed early in the section, that central excess emission is ‘masked’ by intrinsic absorption, and that the increasing radial trend is not a genuine feature of the emitting mechanism.

(d) *Cluster mergers and the soft excess*

A few clusters in this sample, notably the two rich clusters A2142 and A2256, show evidence of recent mergers through asymmetric distributions of X-ray emission. In A2256 there is evidence that soft excess emission is associated with the merging sub-cluster, also of higher X-ray brightness, located to the east of the main brightness peak. In the case of A2142, we find no evidence of soft excess emission associated with the bright south-western irregular quadrant. In both cases the excess X-ray brightness associated with the putative merging event can be due to extra thermal radiation from the merging group; but it is also easily explained with a non-thermal power-law, encompassing 0.2-2 keV luminosities of same order as the thermal luminosity in those regions, see Tables 6 and 7. Following the latter

interpretation, a cluster in the early merger phases may develop significant X-ray excess emission through acceleration of relativistic electrons at strong merger shocks (e.g., Fujita and Sarazin 2001). A few Giga-years after the primary acceleration, the merging subcluster tends to virialize and to assume a more isotropic X-ray brightness distribution; at the same time, relativistic electrons undergo severe interim losses (e.g., Lieu et al. 1999; Ip and Axford 1985) which preferentially leave relic electrons in the  $\Gamma \sim 200$ -400 Lorentz factor range, distributed over larger volumes than the original acceleration sites. The relic electrons emit IC radiation precisely in the EUV and soft X-ray band, as the energy of emitted photons relates to the electron Lorentz factor via the relationship

$$\Gamma = \left( \frac{3\epsilon}{4\epsilon_{MWB}} \right)^{\frac{1}{2}} \quad (3)$$

where  $\epsilon$  is emitted energy, and  $\epsilon_{MWB}$  is the average energy of a MWB photon. The soft excess may therefore be the effect of a merging event occurred a few Giga-years ago, as also shown in detail by Lieu et al. (1999) for the Coma cluster.

(e) *Warm-hot intergalactic filaments and the soft excess*

A new way of interpretation is provided by recent hydrodynamic simulations of formation and evolution of large-scale structures. General agreement among most researchers is that a large fraction of the current epoch's baryons reside mainly in filamentary structures of a warm-hot intergalactic medium (WHIM), extending for several mega-parsecs with  $T=10^5 - 10^7$  K and overdensities of  $\delta \sim 5 - 200$  relative to the critical density (e.g., Cen and Ostriker 1999). These filaments may in fact converge toward galaxy clusters (e.g., Cen et al. 2001, Dave' et al. 2001). The details of the soft X-ray emission from such filamentary structures heavily depend on their temperature, density and metal abundances, which at the moment can only be predicted within order-of-magnitude ranges. However, a simple estimate indicates that a 1 Mpc length of a  $2 \times 10^{-4} \text{ cm}^{-3}$ ,  $T=3 \times 10^6$  K filament directed towards the observer, yields a free-free surface brightness at 0.25 keV which amounts to  $\sim 10\%$  of that of a typical cluster line of sight encountering a 1 Mpc-long column of hot ICM gas at  $T=10^8$  K and density  $10^{-3} \text{ cm}^{-3}$ . In fact, the critical density (if  $\Omega_0 = 1$  and  $H_0=75 \text{ km s}^{-1} \text{ Mpc}^{-1}$ ) is

$$\rho_{\text{cr}} = \frac{3H_0^2}{8\pi G} = 1 \times 10^{-29} \text{ g cm}^{-3} = 6 \times 10^{-6} \text{ H atoms cm}^{-3}. \quad (4)$$

An overdensity of  $\delta = 30$  implies a H atoms density of  $n_f=1.8 \times 10^{-4} \text{ cm}^{-3}$  (if  $\Omega_b \sim \Omega_M$ ). On the other hand, typical hot ICM gas densities are of the order of  $n_{ICM}=10^{-3} - 10^{-4} \text{ H atoms cm}^{-3}$ . The optically thin free-free emission per unit volume in a given band near frequency  $\nu$  is proportional to

$$E \propto n^2 \times T^{-1/2} e^{-\frac{h\nu}{kT}} \quad (5)$$

where  $kT$  is the temperature of emitting gas, and  $h\nu \sim 0.25 \text{ keV}$  applies to the C-band. As an example, we consider the emission from warm filaments at  $kT=240 \text{ eV}$  ( $T \sim 3 \times 10^6 \text{ K}$ )

and  $n_f=1.8 \times 10^{-4} \text{ cm}^{-3}$  ( $\delta = 30$ ), and emission from an hot ICM medium at  $kT=8.2 \text{ keV}$  and  $n_{ICM}=10^{-3} \text{ cm}^{-3}$ , reminiscent of the Coma cluster. The ratio of filament-to-ICM soft X-ray detected surface brightness is

$$r = \frac{E_f \times D_f}{E_{ICM} \times D_{ICM}} = \frac{D_f \times n_f^2 T_f^{-1/2} e^{-\frac{h\nu}{kT_f}}}{D_{ICM} \times n_{ICM}^2 T_{ICM}^{-1/2} e^{-\frac{h\nu}{kT_{ICM}}}} \quad (6)$$

where  $D_f$  is projected length (in cm) of the filament along the line of sight, and similarly  $D_{ICM}$  is the length of the cluster's H column observed, assumed to have a mean density of  $n_{ICM}$ . For the current example, if we assume  $D_f = D_{ICM}$  (say, 1 or 2 Mpc), the above formula yield  $r=0.09$ , or free-free emission from the warm filament is 9% of the hot ICM emission. Clearly  $r$  is a sensitive function of the filament's temperature, of the gas temperatures and of the extent of the ICM and filament gas columns, which may vary significantly from case to case. Moreover, warm filaments at  $T \sim 10^6 \text{ K}$  may have substantial additional soft X-ray emission in the form of lines, which will increase the ratio  $r$  by a factor of several (e.g., Landini and Monsignori-Fossi 1990).

It is therefore possible that the soft excess emission of many clusters is in fact the result of the detection of WHIM filaments projecting themselves onto the clusters. If the filaments indeed converge toward galaxy clusters, it is possible to surmise that lines of sight toward these sources have a higher probability of intercepting filaments with relatively larger overdensities, and therefore filaments are more easily detectable through their projection onto the central 1-2 Mpc of galaxy clusters. Different filament geometries and alignments with respect to our line of sight may be responsible for the different radial trends of the excess emission reported in this paper.

(f) *Cluster galaxies and the soft excess*

We also entertained the possibility of the soft excess originating from a large number of unresolved, X-ray emitting cluster galaxies, as galaxies of all morphological types are spatially extended sources of X-ray emission (e.g., Fabbiano 1989). Recent high-resolution Chandra observations (Blanton, Sarazin and Irwin 2001; Sarazin, Irwin and Bregman 2001) indicate that X-ray emission from early type (E and S0) galaxies can be resolved into a diffuse 'warm' gas halo at  $kT \sim 0.5 \text{ keV}$ , and a contribution from low mass X-ray binaries (LMXB) and other stellar systems. Late type galaxies, on the other hand, normally lack a diffuse halo, but may host X-ray emitting LMXBs, like in the case of our own Milky Way (e.g., Liu et al. 2000,2001, Fabbiano 1989). The diffuse galactic halo emission is significantly softer than that of the hot ICM; on the other hand, the softness of the LMXB radiation, typically composed of a  $kT \sim 0.25 \text{ keV}$  black-body component and a harder  $\alpha \sim 1.2$  power-law (e.g., Blanton, Sarazin and Irwin 2001), depends on the relative ratio of the two components.



While X-ray bright galaxies can be easily resolved and excluded from the analysis of the diffuse cluster soft X-ray emission, X-ray faint galaxies cannot be identified at the resolution of the present study. X-ray faint galaxies have soft X-ray luminosities of the order of  $\sim 10^{38}$  erg s $^{-1}$  (e.g., Fabbiano, Kim and Trinchieri 1992); this figure requires that several thousand such galaxies be present to explain typical soft excess luminosities of order  $10^{41} - 10^{42}$  erg s $^{-1}$  (Table 3).

Optical studies indicate that the projected galaxy number density distribution in clusters is often well described by a King profile (Dressler 1978):

$$\sigma_{gal}(r) = \sigma_0 \left( 1 + \left( \frac{r}{r_{c,gal}} \right)^2 \right)^{-1} \quad (7)$$

where  $r$  is cluster projected radius and  $r_{c,gal}$  is the galaxy density core radius; its behavior at large radii is  $\propto r^{-2}$ . The X-ray surface brightness of the hot ICM gas, on the other hand, is normally well described by

$$I_{gas}(r) = I_0 \left( 1 + \left( \frac{r}{r_{c,gas}} \right)^2 \right)^{-3\beta + \frac{1}{2}} \quad (8)$$

where  $r_{c,gas}$  is the ICM core radius; since  $\beta=2/3$  in most clusters,  $I_{gas}(r) \propto r^{-3}$  at large radii. The two formulas indicate that the X-ray emission from individual galaxies can be more extended than the hot ICM radiation, and it can therefore potentially explain the larger fractional soft excess emission found at large distances from the cluster's center (Fig. 4).

In summary, the excess soft X-ray emission can in principle be due to a very large number of unresolved, X-ray faint galaxies, through their stellar and diffuse halo emission. It is however necessary to point out two possible shortcomings of this interpretation. Firstly, the very bright excess emission of, e.g., A1795, Coma or A2744, is unlikely explained by this scenario, due to the very large number of required faint galaxies ( $\geq 10,000$ ); as an example, the Coma cluster has a population of only about 500 galaxies within B magnitude  $M_B=16$  (Doi et al. 1995). Secondly, it is found that early type galaxies are more commonly found in the central regions of clusters, while the outskirts are relatively more densely populated by late type galaxies (Doi et al. 1995), generally lacking the very soft X-ray halo. Excess emission at large radial distances would therefore need to originate predominantly by stellar emission (LMXB) in late type galaxies alone.

(g) *Additional considerations*

It is also important to remark that even clusters with similar properties, e.g., Virgo and

Fornax, both nearby and poor, or A1795 and A2199, both with bright cD galaxy at the center, central cooler gas (CF, Table 1) and relaxed X-ray morphology, show different soft excess morphology and luminosity (see Table 3). It is therefore possible that soft excess photons are produced by more than one mechanism.

## 6. Comments on individual clusters

**A21** There is no evidence of either excess absorption or emission.

**A85** Bagchi, Pislar and Lima-Neto (1998) noted two regions of X-ray enhancement in SAX data, and excess X-ray emission is also evident in our PSPC data. One is a *very steep spectrum radio source* (VSSRS, located near R.A.=00 41 34.7, Dec.=−9 22 0.2,  $\sim 5$  arcmin offset from the cluster’s center and size  $\sim 1.75$  arcmin radius), the other region (RADIO2, near R.A.=0 41 48.3, Dec.=−9 28 0.2,  $\sim 8$  arcmin south of the cluster’s center and size 3 arcmin radius) is also related to a radio source. We investigated these two regions by (a) studying separately the C-band emission of the two VSSRS and RADIO2 regions, and that of the remainder of the corresponding annular regions (ann-VSSRS and ann-RADIO2); (b) fitting the X-ray excess emission, above the azimuthal average of the annular region, of VSSR and RADIO2 with a non-thermal power-law spectrum, see Table 4. In case (a), there seems to be C-band excess emission associated with both regions, while little excess is evident in the rest of the annulus; for case (b), the X-ray excess is well fitted by the power-law model, and no further C-band excess is noted. It seems therefore that A85’s soft excess is localized in the two radio emission regions and of non-thermal origin.

**A133** There is clear evidence of soft excess emission in this cluster, from the central regions to  $\sim 500$  kpc, the limiting radius of the PSPC detection.

**A665** A665 is one of the furthest clusters of the sample,  $z=0.182$ , and relatively high HI column density ( $N_H = 4.3 \times 10^{20} \text{ cm}^{-2}$ ). It shows evidence of central absorption, and no soft excess emission.

**A1045** No literature references were available for temperature and abundances of this cluster; PSPC measures a  $T \sim 3\text{-}5$  keV when metal abundances are fixed at  $A=0.3$  solar (Table 3). There is marginal evidence of central excess absorption and no evidence of soft excess emission.

**A1068** Only a  $2\text{-}\sigma$  evidence of soft excess in the regions surrounding the cluster core is evident from our observation.

**A1302** The 2.3 ks PSPC observation is of limited quality, but compatible with soft

Table 4. The soft X-ray properties of the VSSRS and RADIO2 regions of A85, and their azimuthally averaged annuli (A-VSSRS and A-RADIO2)

Region (arcmin)	$\chi_r^2$ (dof)	C-band flux (model) $10^{-2} \text{ c s}^{-1}$	$\alpha$	EM	$L_{nt}/L_{th}$
VSSRS	0.65(57)	$1.75 \pm 0.16$ (1.43)	...	...	...
A-VSSRS	0.82(151)	$11.8 \pm 0.4$ (11.5)	...	...	...
RADIO2	0.63(78)	$2.64 \pm 0.2$ (2.12)	...	...	...
A-RADIO2	0.82(144)	$9.6 \pm 0.48$ (8.9)	...	...	...
VSSRS XE	0.7(70)	...	$1.54 \pm_{0.15}^{0.21}$	$\sim 14.2$	$\sim 1.0$
RADIO2 XE	0.64(99)	...	$1.5 \pm_{0.14}^{0.11}$	$\sim 12.8$	$\sim 2.2$

Note. — ‘EM’ indicates by how many times the normalization constant of the spectrum (the Emission Measure) exceeds the prediction from the annular average, ‘XE’ means X-ray excess.  $L_{nt}/L_{th}$  is the ratio of non-thermal to thermal luminosity in 0.2-2 keV band. Hot ICM is modeled with a kT=7 keV, A=0.3 MEKAL model at all radii, HI column density is  $N_H = 2.5 \times 10^{20} \text{ cm}^{-2}$ .

excess emission of order 10-50% outside the central 100 kpc, inward of which the C-band radiation is on par with the hot ICM.

**A1314** The very short PSPC exposure (2 ks) of this poor but very nearby cluster indicates, although within large statistical error bars, that A1314 may host soft excess emission, throughout the central  $\sim 500$  kpc where cluster emission is detected.

**A1361** The 3.9 ks PSPC exposure constrains the C-band excess emission of this cluster to  $\sim +20 \pm 20\%$  outside the central 100 kpc.

**A1367** A1367 is an X-ray faint and very nearby galaxy cluster, near the brighter Coma cluster. It has a secondary peak of the X-ray brightness (Donnelly et al., 1998), which we study here separately. The secondary peak is located near R.A.=11 44 21.7, Dec.=+19 52 13.2, approximately 19 arcmin offset from the primary brightness peak. While azimuthally averaged annuli around the primary peak revealed no evidence of soft excess emission (see Fig. 1), the secondary peak (divided into 0-3 and 3-6 arcmin regions from its center) seems associated with soft excess emission, see Fig. 9 and Table 5.

**A1413** At  $z=0.14$ , this cluster reveals marginal excess emission between 0.1-1 Mpc, at a level not exceeding  $\sim 30\%$ .

**A1689** This cluster has no clear evidence of soft excess emission.

**A1795** A1795 is known to have soft excess emission from *EUVE*/DS observations (Bonamente, Lieu and Mittaz 2001b). The *EUVE* excess was more prominent at large radii (see e.g., Fig. 4 of Bonamente, Lieu and Mittaz 2001b) while the PSPC data analyzed here shows soft X-ray excess emission extending from the central regions to the limits of the C-band detection, at the level of  $\eta = 10-20\%$ . There is no evidence of C-band excess absorption in this analysis of PSPC data.

**A1914** This clusters shows a very similar behavior to A1361, with possible soft excess emission not to exceed  $\sim 20-30\%$ .

**A1991** There is evidence of excess absorption in the center and marginal soft excess in the outskirts of this X-ray faint cluster.

**A2029** This X-ray bright and rich cluster shows evidence (at  $\sim 3 - 4\sigma$  level) of soft excess emission outside its central 100 kpc, at level of 10%.

**A2142** A2142 shows a clear enhancement of the X-ray emission in the south-eastern quadrant (Briel and Henry 1996). We investigated the properties of the emission in that region, and how it compares with the emission in the remainder of the azimuthal directions (see Fig. 9 and Table 6).

Table 5. Soft X-ray properties of the secondary brightness peak of A1367.

Region (arcmin)	$\chi_r^2$ (dof)	C-band flux (model) $10^{-2} \text{ c s}^{-1}$	$L_{NT}$ $10^{41} \text{ erg s}^{-1}$	$L_{therm}$ $10^{41} \text{ erg s}^{-1}$
0-3 peak2	1.04(71)	$2.8 \pm 0.16$ (2.4)	$0.54 \pm_{0.54}^{1.7}$	$0.32 \pm 0.24$
3-6 peak2	1.05(119)	$5.96 \pm 0.25$ (5.36)(55%)	$1.1 \pm_{0.9}^{0.8}$	$0.49 \pm_{0.37}^{0.35}$

Note. — The hot ICM emission is modeled with a  $kT=4.2$  keV,  $A=0.2$  solar and HI column density  $N_H = 1.7 \times 10^{20} \text{ cm}^{-2}$  photoabsorbed MEKAL model. See caption of Table 3 for definition of  $L_{NT}$  and  $L_{therm}$ .

Table 6. Soft X-ray properties of the south-eastern quadrant of A2142 (3-6-SE and 6-9-SE) and of the remainder of the azimuthal directions (ann-3-6 and ann-6-9)

Region (arcmin)	$\chi_r^2$ (dof)	C-band flux (model) $10^{-2} \text{ c s}^{-1}$	$L_{NT}$ $10^{41} \text{ erg s}^{-1}$	$L_{therm}$ $10^{41} \text{ erg s}^{-1}$	$\alpha$	EM	$\frac{L_{nt}}{L_{th}}$
ann-3-6	0.81(151)	$3.1 \pm 0.19$ (2.54)	$6.4 \pm_{6.4}^{20}$	$12 \pm_{12}^9$	...	...	...
3-6-SE	0.69(151)	$2.05 \pm 0.15$ (2.16)	...	...	...	...	...
ann-6-9	0.75(114)	$1.1 \pm 0.18$ (1.44) (23%)	...	...	...	...	...
6-9-SE	0.53(99)	$1.05 \pm 0.14$ (1.14) (46%)	...	...	...	...	...
3-6-SE XE	0.73(179)	...	...	...	$1.3 \pm_{0.12}^{0.1}$	2.5	1.35
6-9-SE XE	0.58(115)	...	...	...	$1.27 \pm_{0.2}^{0.18}$	2.4	1.4

Note. — The X-ray excess emission (‘XE’) is also modeled with a non-thermal power-law, see caption of Table 4 for details. The hot ICM emission is modeled with a  $kT=9$  keV,  $A=0.3$ ,  $N_H = 4.2 \times 10^{20} \text{ cm}^{-2}$  photoabsorbed MEKAL model for all regions. See caption of Table 3 for definition of  $L_{NT}$  and  $L_{therm}$ .

There is marginal evidence of soft excess emission in the central 500 kpc of this clusters, detected out to a radius of  $\sim 1$  Mpc. The south-eastern quadrant’s X-ray excess (above the azimuthal average) can be successfully modeled with a power-law model, indicating a possible non-thermal origin of the X-ray excess brightness.

**A2199** A2199 has marginal evidence of soft excess emission in this deep PSPC observation. *EUVE* data (Lieu, Bonamente and Mittaz 1999; Bonamente, Lieu and Mittaz 2001b) show significant extreme-ultraviolet excess that reaches an importance of a few times 100% at large distances from the center. The only possibility to reconcile the two observations is that the soft excess emission in this source is mainly confined to energies below  $\sim 0.2$  keV.

**A2218** There is evidence of soft excess emission at the level of  $\sim 20\%$  in the PSPC observation of this very rich,  $z=0.171$  cluster.

**A2219** The 8.5 ks observation of this  $z=0.23$  cluster indicate that soft excess emission may be present at the 20-30% level in the regions surrounding the cluster’s core, although is presently detected with low statistical significance.

**A2241** There is evidence of excess absorption in the central  $\sim 100$  kpc of this cluster, which is detected only out to a radius of  $\sim 300$  kpc.

**A2244** The short PSPC exposure detects no evidence of excess C-band emission/absorption.

**A2255** There is evidence of soft excess emission in the regions immediately surrounding the core and, with marginal S/N, at the cluster’s outskirts.

**A2256** The X-ray emission of this cluster shows an asymmetry in the western quadrant (approximately 90 degrees wide, positioned 20 degrees west of north to 20 degrees south of west, e.g., Briel et al. 1991, Sun et al. 2002), presumably associated with merger activity. Concentric annuli are accordingly divided in two sectors, ‘W’ being the western quadrant, and the remainder of the azimuthal directions, to further study the C-band emission (Table 7). The marginal soft excess emission detected in the whole cluster seems associated only with the narrow quadrant of asymmetric X-ray distribution, where it is detected with large S/N, see Fig. 9. In addition, the excess X-ray emission in W above the azimuthal average of the remainder of azimuthal directions, of lower X-ray brightness, is modeled with a non-thermal model. The excess X-ray component in 0-6 and 6-9 arcmin regions of W is also successfully modeled with a second thermal component at  $T \sim 1.7 - 1.8$  keV.

**A2597** The soft excess emission is strongly detected only in the 1-3 arcmin region, while the C-band signal is consistent with hot ICM prediction in the inner and outermost regions.

**A2670** Hobbs and Willmore (1997) indicate that this cluster has evidence of merger

Table 7. The soft X-ray properties of A2256 in western quadrant (W) and in the remainder of the azimuthal directions

Region (arcmin)	$\chi_r^2$ (dof)	C-band flux (model) $10^{-2}$ c s $^{-1}$	$L_{NT}$ $10^{41}$ erg s $^{-1}$	$L_{therm}$ $10^{41}$ erg s $^{-1}$	$\alpha$	EM	$\frac{L_{nt}}{L_{th}}$
ann-0-3	1.1(138)	3.1 $\pm$ 0.15 (3.29)	...	...	...	...	...
ann-3-6	1.04(141)	3.32 $\pm$ 0.18 (3.8)	...	...	...	...	...
ann-6-9	1.07(131)	2.31 $\pm$ 0.18 (2.39)	...	...	...	...	...
ann-9-12	0.83(110)	0.83 $\pm$ 0.18 (1.1) (11%)	...	...	...	...	...
0-6 W	1.37(136)	4.7 $\pm$ 0.18 (3.8)	65 $\pm$ $_{13}^{11}$	23 $\pm$ $_{6.5}^{7.2}$	...	...	...
6-9 W	0.92(98)	1.5 $\pm$ 0.12 (1.17)	22 $\pm$ 10.5	7.6 $\pm$ $_{3.9}^{4.5}$	...	...	...
0-6 XE	1.0(164)	...	...	...	1.8 $\pm$ $_{0.1}^{0.06}$	1.5	0.7
6-9 XE	0.86(116)	...	...	...	1.8 $\pm$ $_{0.4}^{1.1}$	1.4	0.4

Note. — See caption of Table 4 for details. The hot ICM emission is modeled with a kT=7 keV, A=0.3 and  $N_H = 4.6 \times 10^{20}$  cm $^{-2}$  photoabsorbed MEKAL model. See caption of Table 3 for definition of  $L_{NT}$  and  $L_{therm}$ .

activity. It is strongly absorbed in the central  $\sim 200$  kpc, and only marginal evidence of excess outwards.

**A2717** There is no evidence of either excess emission or absorption in this cluster.

**A2744** The most distant cluster of this sample ( $z=0.31$ , Abell richness class 3) has clear evidence of strong soft excess emission in our 13.8 ks PSPC observation, at the level of  $\sim 50\%$ . The cluster is a strong X-ray emitter, and is detected out to a radius of  $\sim 2$  Mpc. Detected soft excess emission implies thermal and non-thermal luminosities of order  $10^{43}$  erg  $s^{-1}$  in 0.2-0.4 keV band, see Table 3, the highest to date.

**A3301** A3301 has only marginal evidence of soft excess emission in the regions outwards of  $\sim 50$  kpc.

**A3558** The strong soft X-ray excess of A3558 was already reported by Bonamente et al. (2001c); the excess reaches  $\sim 30\%$  importance with respect to the hot ICM.

**A3560** There is only marginal evidence of excess emission; the PSPC exposure achieves only limited S/N.

**A3562** The soft excess of this cluster is revealed with good statistical confidence in the  $\sim 400$  kpc region of the PSPC detection (see also Bonamente et al. 2001c).

**A3571** A3571 has a  $\sim 20\%$  soft excess emission extending across the entire cluster extent. A pointed BeppoSAX observation (Bonamente et al. 2001c) reports the matching LECS 0.15-0.3 keV excess.

**A4059** There is no evidence of soft X-ray excess, and only marginally of intrinsic absorption in the center.

**Coma** The Coma cluster had its soft excess emission discovered originally with *EUVE* (Lieu et al. 1996b), and this PSPC observation confirms the excess emission with very large statistical significance. The PSPC excess has an importance of  $\sim 20\text{-}30\%$  of the hot ICM throughout the limits of our analysis (18 arcmin radius).

**Fornax** This is a poor and very nearby cluster ( $z=0.0046$ ). The deep PSPC observation (53 ks) shows strong soft excess emission that reaches a 50% importance (see also Rangarajan et al. 1995), with a radial trend resembling closely that of Sérsic 159-03 (Bonamente, Lieu and Mittaz 2001d), although X-ray emission is detected out to a radial distance of only  $\sim 100$  kpc from the cluster's center.

**Hercules** The Hercules cluster of galaxies (also known as A2151) has faint X-ray emission. It shows two peaks of the X-ray intensity (see Bird et al. 1995, and Huang and Sarazin



1996), which we investigated separately in Fig. 2. There is only marginal evidence of soft excess emission in the brightest of the two peaks.

**Virgo** Along with Coma, it was one of the two clusters where the soft excess emission was initially discovered, in a deep *EUVE* observation (Lieu et al. 1996a). The PSPC excess emission, already reported also in Bonamente, Lieu and Mittaz (2001b), is strongly detected with  $\eta \sim 0.3$ -0.4 throughout the limits of this investigation (18 arcmin radius). This cluster is at very low redshift ( $z=0.0043$ ), similar to that of the Fornax cluster; it shows a rather flat radial trend of the soft excess, completely different from that of Fornax over the same interval of radii ( $\sim 0$ -100 kpc).

## 7. Conclusions

The PSPC observations analyzed in this paper show excess soft X-ray radiation (0.2-0.4 keV) in a large fraction of the sources, proving that the thermal radiation from the hot ICM is not solely responsible for the majority of cluster soft X-ray spectra. The main indication as to the nature of the excess emission is provided by the preferential presence at large cluster radii, suggesting a non-thermal nature of the phenomenon. An alternative explanation would require a ‘warm’ ICM phase, although its short cooling time necessitates a source of re-heating. The latter requirement may however be avoided if the soft X-ray excess originates from the emission of warm, lower density large-scale filamentary structures impinging on the clusters.

The authors thank Dr. E.M. Murphy for making his data available ahead of publication and Dr. Osmi Vilhu for helpful discussions. MB and RL thank NASA for support.

### Figure captions

Figure 1: The fractional excess  $\eta$  for each cluster, see Eq. 1, averaged over all cluster regions where C-band emission exceeds 25% of the background, see Table 1.

Figure 2: The radial distribution of the fractional soft X-ray excess emission/absorption  $\eta$  for each cluster, as function of distance from the cluster’s center (bottom axis: Arcmin; top axis: Mpc). Vertical semidiameters are  $1\text{-}\sigma$  errors which include statistical and model uncertainties (see text). Dotted diamonds are regions where C-band emission is below 25% of the C-band background; where no dotted diamonds are reported, either the PSPC boresight position did not allow to extend the analysis to larger radii (A1367, Coma and Virgo), or the peculiar cluster morphology impeded it (Hercules).

Figure 3: Composite  $\eta$  distribution of all cluster regions as function of radial distance. Each data point represents an annular region at its mean radius, horizontal error bars are omitted for clarity. Errors are  $1\text{-}\sigma$  uncertainties.

Figure 4: The cumulative distribution of  $\eta$  for all regions (top;  $\langle \eta \rangle = 0.088$ , variance  $\sigma_\eta = 0.167$ ), only regions at a mean distance  $\leq 0.17$  Mpc from the cluster center (middle;  $\langle \eta \rangle = 0.024$ ,  $\sigma_\eta = 0.057$ ) and regions at mean distance  $\geq 0.17$  Mpc (bottom;  $\langle \eta \rangle = 0.131$ ,  $\sigma_\eta = 0.202$ ).

Figure 5: Composite  $\eta$  distribution of all cluster regions as function of X-ray core radius, see Table 1.

Figure 6: Composite  $\eta$  distribution of all cluster regions as function of detector radial distance from boresight.

Figure 7: Composite  $\eta$  distribution of all cluster regions as function of Galactic HI column density, see Table 1.

Figure 8: Composite  $\eta$  distribution of peripheral cluster regions where C-band counts are  $\leq 25\%$  of C-band background.

Figure 9: Left: the  $\eta$  distribution in concentric annuli of A1367 around the primary brightness peak (solid diamonds) and around the secondary peak (dashed diamonds). Middle: the  $\eta$  distribution of A2142 in concentric annuli (solid diamonds, as in Fig. 2), and separately in south-western quadrant (dashed diamonds) and remainder of azimuthal directions (dot-dashed diamonds). Right: the  $\eta$  distribution of A2256 (solid diamonds, as in Fig. 2) and separately in eastern quadrant (dot-dashed diamonds) and remainder of azimuthal directions (dashed diamonds).

## REFERENCES

- Allen, S.W. 2000, MNRAS, 315, 269
- Allen, S.W., Fabian, A.C., Johnston, R.M., Arnaud, K.A. and Nulsen, P.E.J. 2001, MNRAS, 322, 589
- Allen, S.W., Fabian, A.C., Edge, A.C., Böhringer, H. and White, D.A. 1995, MNRAS, 275, 741
- Arnaud, M., Neumann, D. M., Aghanim, N., Gastaud, R., Majerowicz, S. and Hughes, J. P. 2001, A&A, 365, L80

- Bagchi, J., Pislak, V. and Lima Neto, G.B. 1998, MNRAS, 296, 23
- Berghoefer, T.W., Bowyer, S., & Korpela, E.J., 2000, ApJ, 545, 695
- Berghoefer, T.W., Bowyer, S., & Korpela, E.J., 2000, ApJ, 535, 615
- Bird, C.M., Davis, D.S. and Beers, T.C. 1995, AJ, 109, 920
- Blanton, E.L., Sarazin, C.L. and Irwin, J.A. 2001, ApJ, 552, 119
- Boehringer, H., Matsushita, K., Churazov, E., Ikebe, Y. and Chen, Y. 2002, A&A, 382, 804
- Bonamente, M., Lieu, R. and Mittaz, J.P.D. 2001a, ApJ, 546, 805
- Bonamente, M., Lieu, R. and Mittaz, J.P.D. 2001b, ApJ, 547,L7
- Bonamente, M., Lieu, R. , Nevalainen, J. and Kaastra, J.S. 2001c, ApJ, 552,L7
- Bonamente, M., Lieu, R. and Mittaz, J.P.D. 2001d, ApJ, 561, L67
- Bonamente, M. 2000, *Ph.D. Thesis*, University of Alabama in Huntsville
- Boulanger, F. and Perault, M. 1988, ApJ, 330, 964
- Bowyer, S., Berghoeffer, T.W. 1998, ApJ, 506, 502
- Bowyer, S., Berghoeffer, T.W., and Korpela, E.J., 1999, ApJ, 526, 592
- Bowyer, S., Korpela, E.J., & Berghoefer, T.W., 2001, ApJ, 548, L135
- Briel, U.G. and Henry, J.P. 1996, ApJ, 472, 131
- Briel, U.G., Henry, J.P, Schwartz, R.A., Böhringer, H., Ebeling, H., Edge, A.C., Hartner, G.D., Schindler, S., Trümper, J. and Voges, W. 1991, A&A, 246, L10
- Buote, D.A., 2000a, ApJ, 544, 242
- Buote, D.A., 2000b, ApJ, 532, L113
- Buote, D.A., 2001, ApJ, 548, 652
- Cen, R. and Ostriker, J.P. 1999, ApJ, 514, L1
- Cen, R., Tripp, T.M., Ostriker, J.P. and Jenkins, E.B. 2001, ApJ, 559,L5
- Dave', R., Cen, R., Ostriker, J.P., Bryan, G.L., Hernquist, L., Katz, N., Weinberg, D.H., Norman, M.L. and O'Shea, B. 2001, ApJ, 552, 473

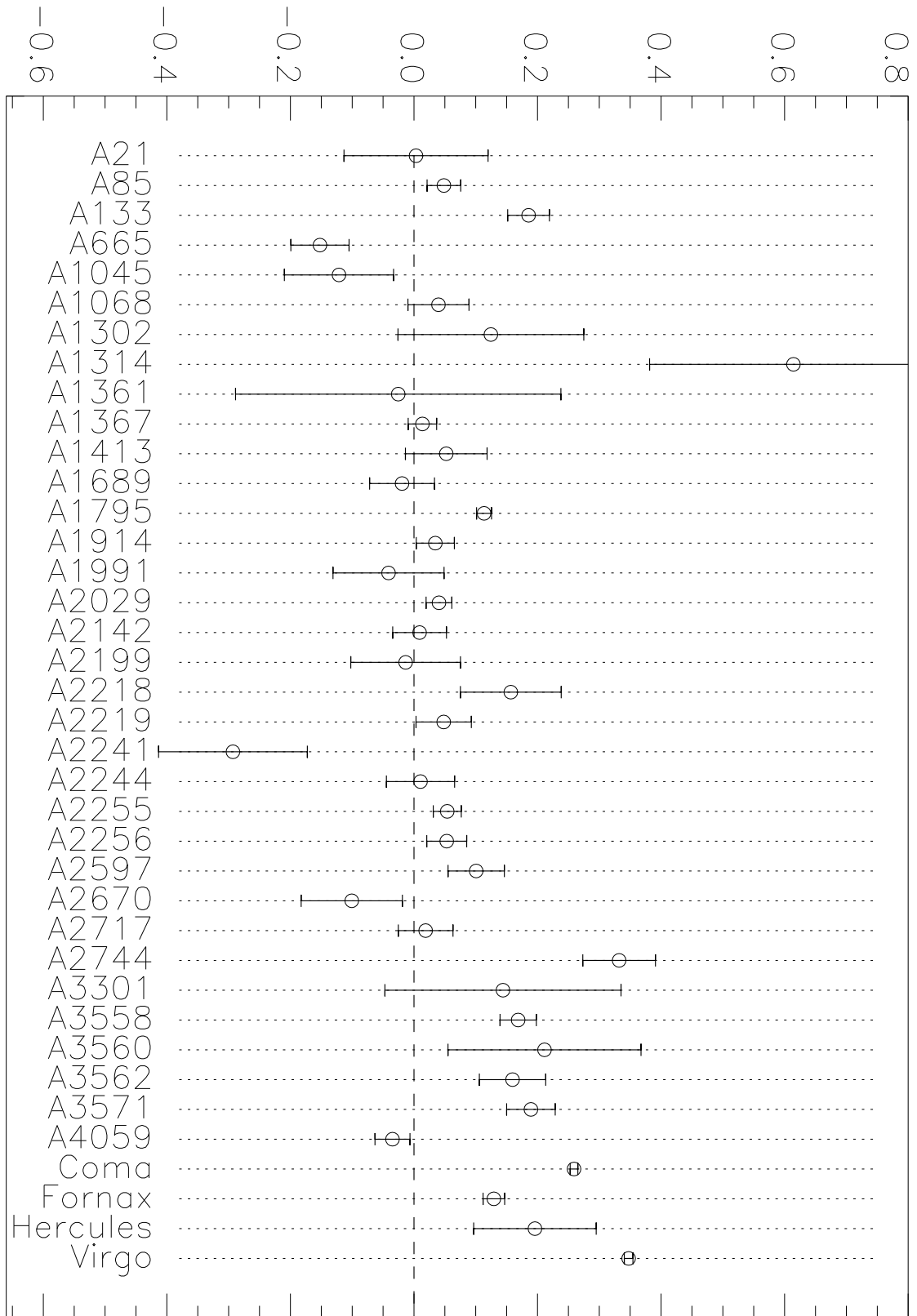
- De Grandi, S. and Molendi, S. 2002, ApJin press
- De Grandi, S. and Molendi, S. 2001, ApJ, 551, 153
- Dickey, J.M. and Lockman, F.J. 1990, ARA&A, 28, 215
- Dixon, W.V., Sallmen, S., Hurwitz, M., & Lieu, R., 2001, ApJ, 550,L25
- Dixon, W.V., Hurwitz, M., & Ferguson, H.C., 1996, ApJ, 469, L77
- Doi, M., Fukugita, M, Okamura, S. and Turner, E.L. 1995, AJ, 109, 1490
- Donnelly, R.H., Markevitch, M., Forman, W., Jones, C., David, L.P., Churazov, E. and Gilfanov, M. 1998, ApJ, 500, 138
- Dressler, A. 1978, ApJ226 55
- Ebeling, H., Voges, W., Böhringer, H., Edge, A.C., Huchra, J.P. and Briel, U.G. 1996, MNRAS, 281, 799
- Elvis, M., Lockman, F.J. and Wilkes, B.J. 1989, AJ, 97,777
- Fabbiano, G. 1989, ARA&A, 27, 87
- Fabbiano, G., Kim, D.-W. and Trinchieri, G. 1992, ApJS, 80, 531
- Fabian, A.C. 1988, Cooling flows in clusters and galaxies, Kluwer
- Fabian, A.C. 1996, Science, 271, 1244
- Fujita, Y. and Sarazin, C.L. 2001, ApJ, 563, 60
- Fusco-Femiano, R., Dal Fiume, D., De Grandi, S., Feretti, L., Giovannini, G., Grandi, P., Malizia, A., Matt, G., Molendi, S. 2000, ApJ, 534, L7
- Henry, J.P. and Briel, U.G. 1996, ApJ, 472, 137
- Hobbs, I.S. and Willmore A.P. 1997, MNRAS, 289, 685
- Huang, Z. and Sarazin, C.L. 1996, ApJ, 461, 625
- Ikebe, Y., Reiprich, T.H., Böhringer, H., Tanaka, Y. and Kitayama, T. 2002, A&Ain press
- Ip, W.-H. and Axford, W.I. 1985, A&A, 149, 7
- Irwin, J.A. and Bregman, J.N. 2000, ApJ, 538, 543

- Jones, C., Stern, C., Forman, W., Breen, J., David, L. and Tucker, W. 1997, ApJ, 482, 143
- Kaastra, J.S. 1992 in An X-Ray Spectral Code for Optically Thin Plasmas (Internal SRON-Leiden Report, updated version 2.0)
- Kaastra, J.S., Lieu, R., Mittaz, J.P.D., Bleeker, J. A. M., Mewe, R., Colafrancesco, S. and Lockman, F. J. 1999, ApJ, 519, L119
- Landini, M. and Monsignori-Fossi B.C. 1990, A&A, 82, S229
- Laor, A., Fiore, F., Elvis, M., Wilkes, B and McDowell, J.C. 1994, ApJ, 435, 611
- Liang, H., Pierre, M., Unewisse, A. and Hunstead, R.W. 1997, A&A, 321,64
- Lieu, R., Mittaz, J.P.D., Bowyer, S., Lockman, F.J., Hwang, C. -Y., Schmitt, J.H.M.M. 1996a, ApJ, 458, L5
- Lieu, R., Mittaz, J.P.D., Bowyer, S., Breen, J.O., Lockman, F.J., Murphy, E.M. & Hwang, C. -Y. 1996b, Science, 274,1335
- Lieu, R., Bonamente, M., Mittaz, J.P.D., Durret, F., Dos Santos, S. and Kaastra, J. 1999a, ApJ, 527,L77
- Lieu, R., Bonamente, M. and Mittaz, J.P.D. 1999, ApJ, 517, L91
- Lieu, R., Bonamente, M., & Mittaz, J.P.D., 2000, A&A,364, 497
- Lieu, R., Ip, W.-I., Axford, W.I. and Bonamente, M. 1999, ApJ, 510,L25
- Lima Neto, G.N., Pislár, V. and Bagchi, J. 2001, A&A, 368,440
- Liu, Q. Z., van Paradijs, J., van den Heuvel, E. P. J. 2001, A&A368 1021
- Liu, Q. Z., van Paradijs, J., van den Heuvel, E. P. J. 2000, A&A147 S25
- Markevitch, M., Vikhlinin, A., Forman, W.R. and Sarazin, C.L. 1999, ApJ,527,545
- Markevitch, M. Forman, W.R., Sarazin, C.L. and Vikhlinin, A. 1998, ApJ,503,77
- Mewe, R., Gronenschild, E.H.B.M., and van den Oord, G.H.J., 1985 A&A,62, S197
- Mewe, R., Lemen, J.R., and van den Oord, G.H.J. 1986, A&A, 65, S511
- Mittaz, J.P.D., Lieu, R. and Lockman, F.J. 1998, ApJ, 498, L17
- Mohr, J.J., Mathiesen, B. and Evrard, A.E. 1999, ApJ, 517, 627

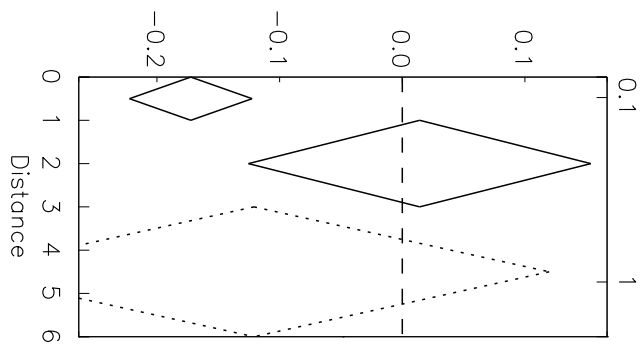
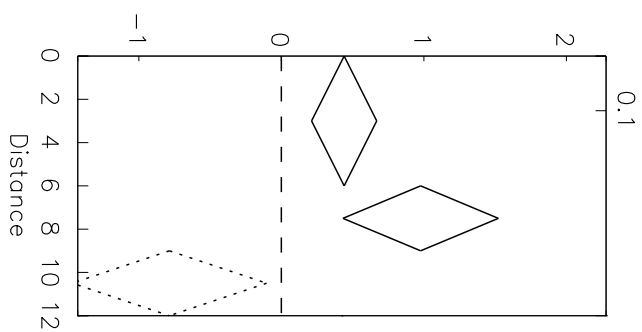
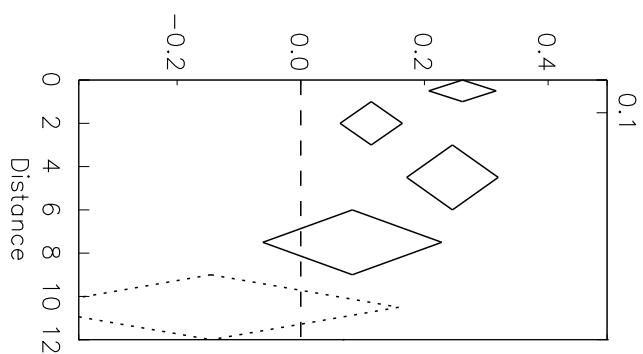
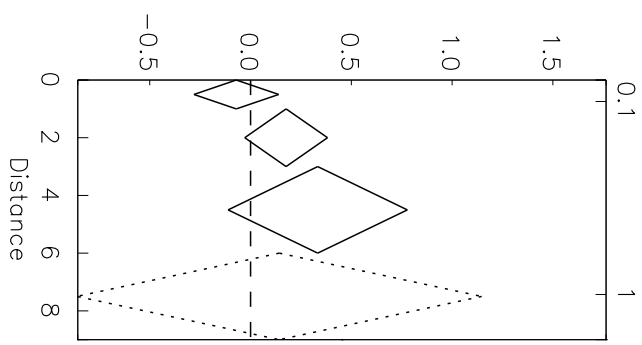
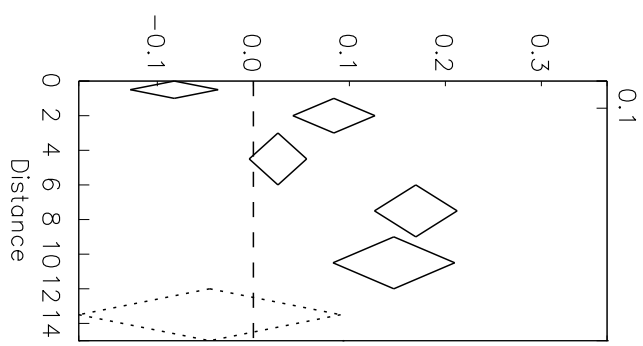
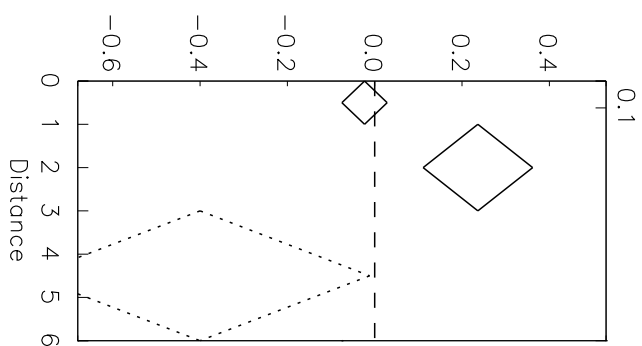
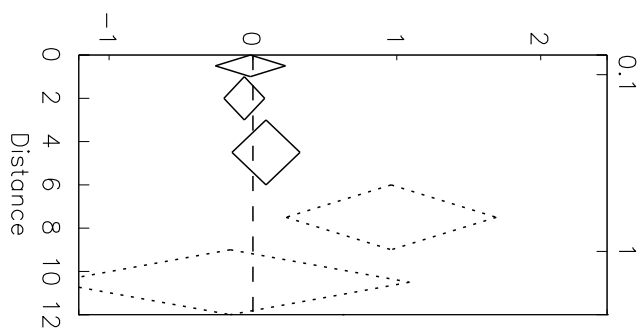
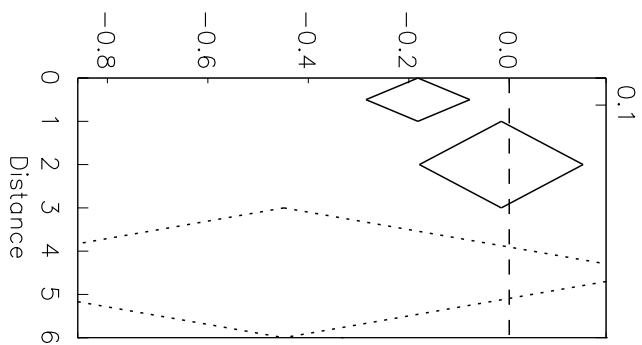
- Neumann, D.M. and Böhringer H. 1999, ApJ, 512, 630
- Peres, C.B., Fabian, A.C., Edge, A.C., Allen, S.W., Johnston, R.M. and White, D.A. 1998, MNRAS, 298, 416
- Plucinsky. P.P., Snowden, S.L., Briel, U.G., Hasinger, G. and Pfeffermann, E. 1993, ApJ, 418, 519
- Rangarajan, F.V.N., Fabian, A.C., Forman, W.R. and Jones, C. 1995, MNRAS, 272, 665
- Reichert, G., Mason, K.O., Lea, S.M., Charles, P.A., Bowyer, S. and Pravdo, S. 1981, ApJ, 247, 803
- Reynolds, A.P, Parmar, A. N., Hakala, P. J., Pollock, A. M. T., Williams, O. R., Peacock, A. and Taylor, B. G. 1999, A&A, 134, S287
- Morrison, R. and McCammon, D. 1983, ApJ, 270, 119
- Sarazin, C.L. and Lieu, R. 1998, ApJ, 494, L177
- Sarazin, C.L., Irwin, J.A and Bregman, J.N. 2001, ApJ, 556, 533
- Schwoppe, A., Hasinger, G., Lehmann, I., Schwarz, R., Brunner, H., Neizvestny, S., Ugryumov, A., Balega, Y., Trümper, J and Voges, W. 2000, Astr. Nach., 321, 1
- Siddiqui, H., Stewart, G.C. and Johnston, R.M. 1998, A&A, 334, 71
- Snowden, S.L., Egger, R., Finkbeinder, D.P., Freyberg, M.J. and Plucinsky, P.P. 1998, ApJ, 493, 715
- Snowden, S.L., McCammon, D., Burrows, D.N. and Mendenhall, J.A. 1994, ApJ, 424, 714
- Sun, M., Murray, S. S., Markevitch, M. and Vikhlinin, A. 2002, ApJ, 565, 867
- Valinia, A. Arnaud, K., Loewenstein, M., Mushotzky, R. F. and Kelley, R. 2000, ApJ, 541, 550
- Yan, M., Sadeghpour, H.R. and Dalgarno, A. 1998, ApJ, 496, 1044
- White, D.A. 2000, MNRAS, 312, 663
- White, D.A., Jones, C. and Forman, W. 1997, MNRAS, 292, 419
- Wilms, J., Allen, A. and McCray R. 2000, ApJ, 542, 914

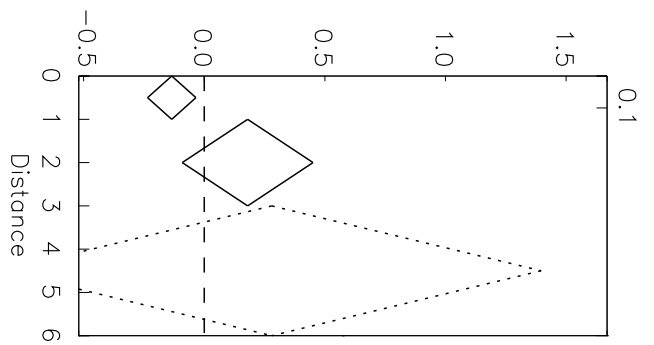
Wheelock, S. et al., 1994, IRAS Sky Survey Expl. Supp., (IPL Publ. 94-11), Pasadena, CA.

average fractional excess

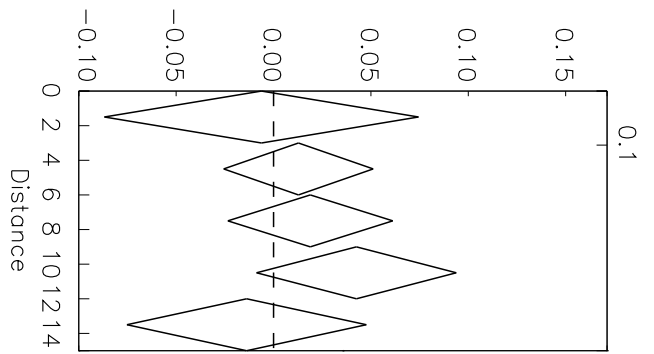




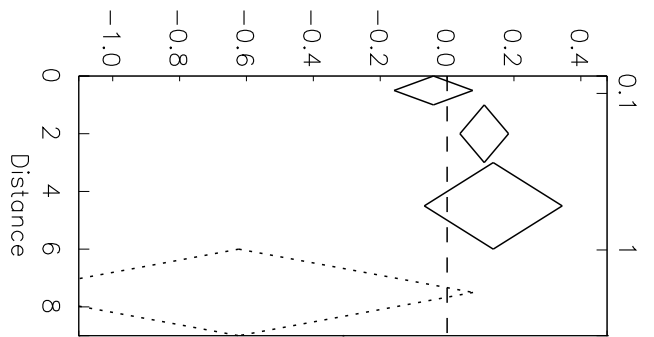




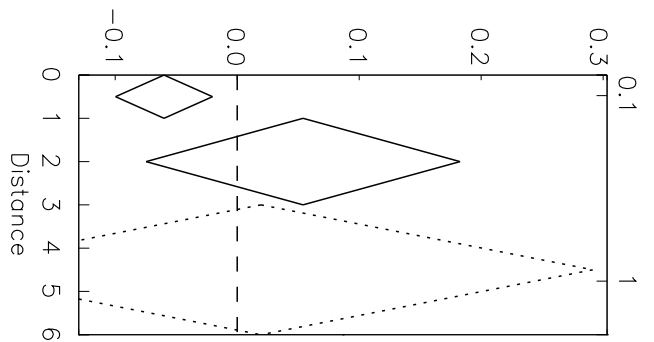
A1361



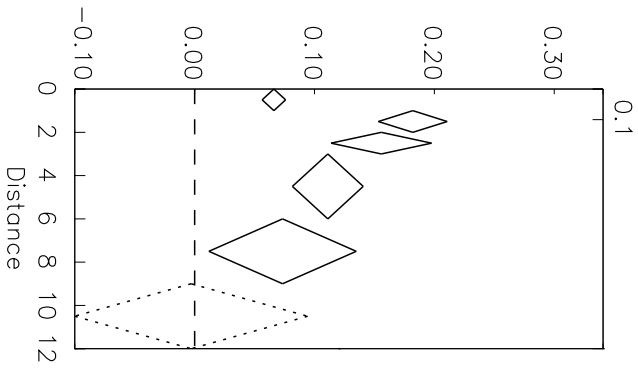
A1367



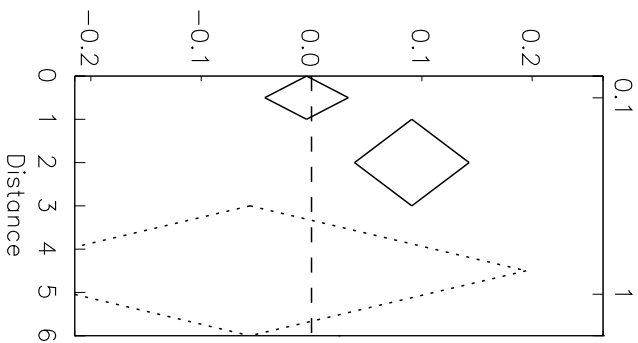
A1413



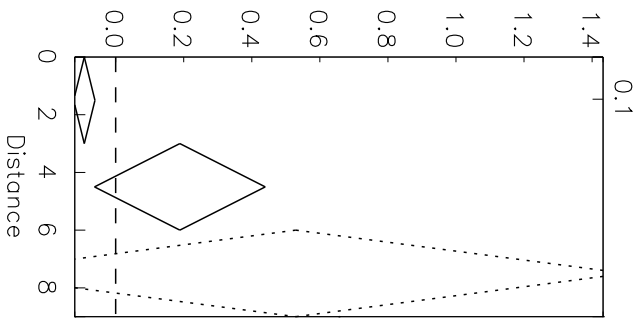
A1689



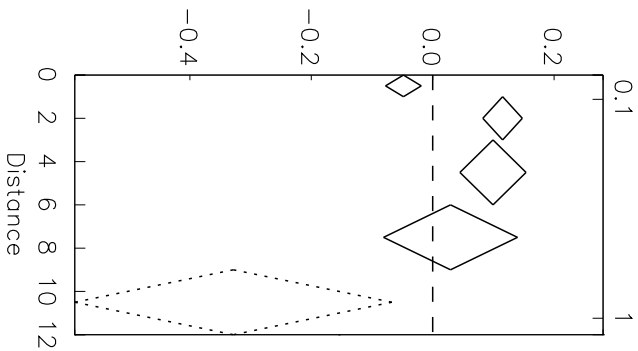
A1795



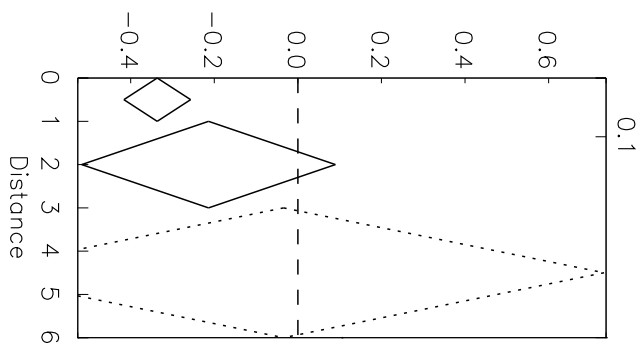
A1914



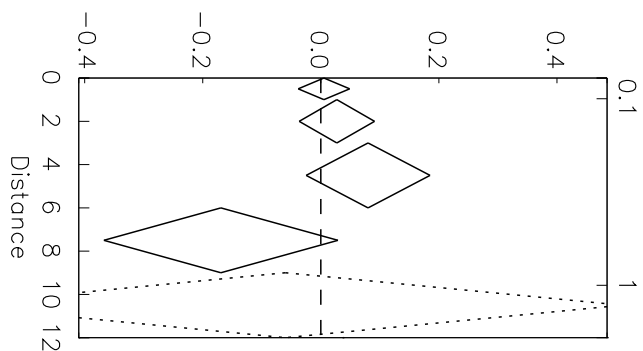
A1991



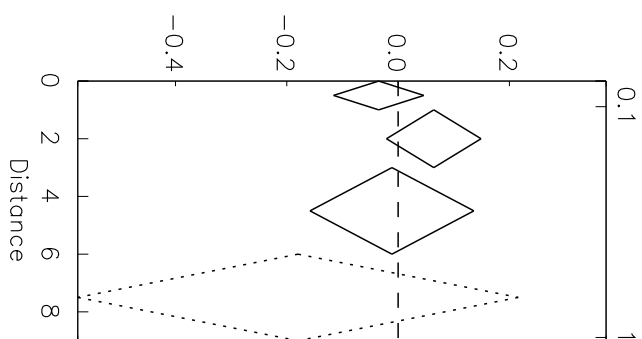
A2029



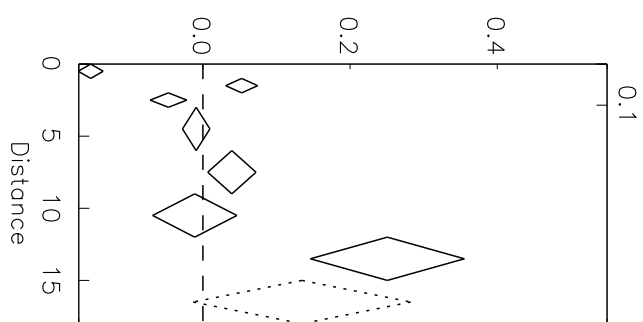
A2241



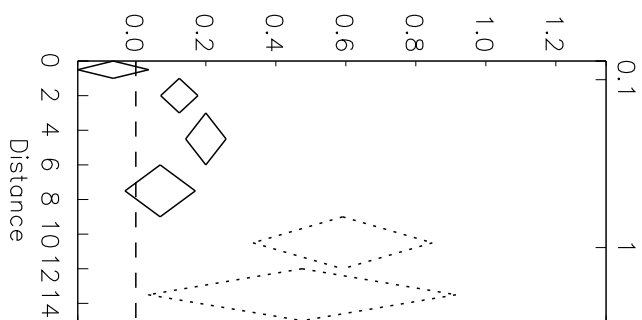
A2142



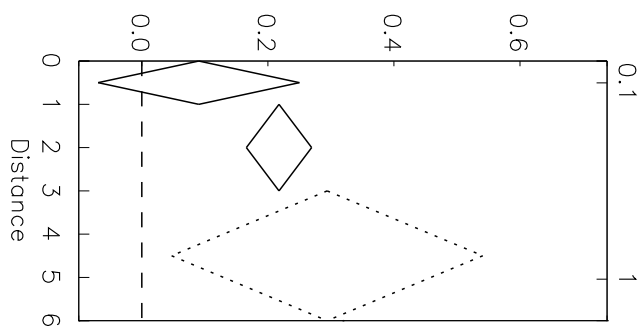
A2244



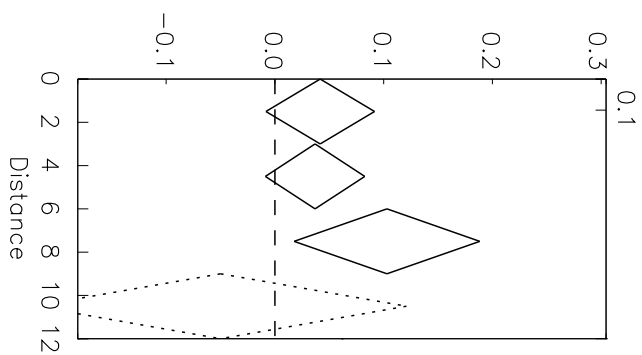
A2199



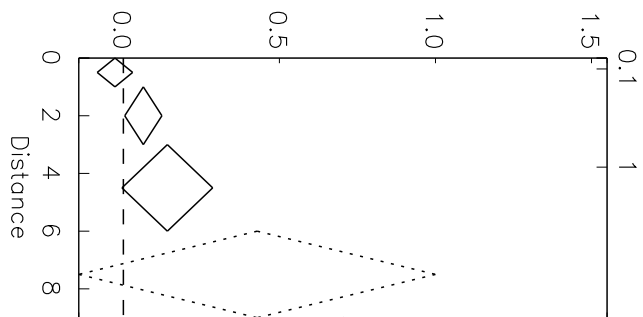
A2255



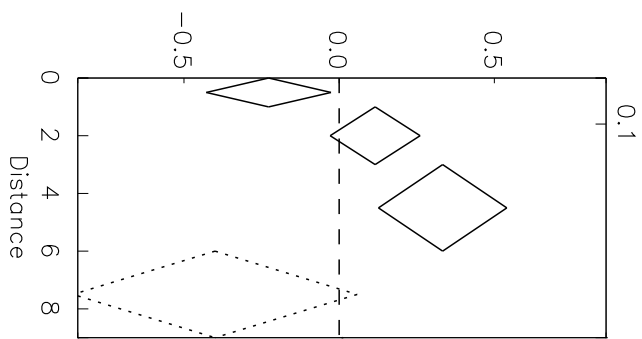
A2218



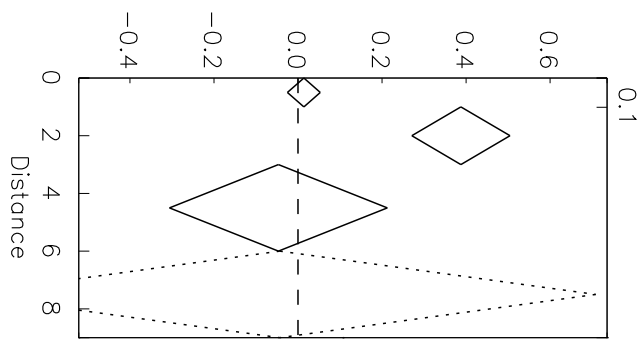
A2256



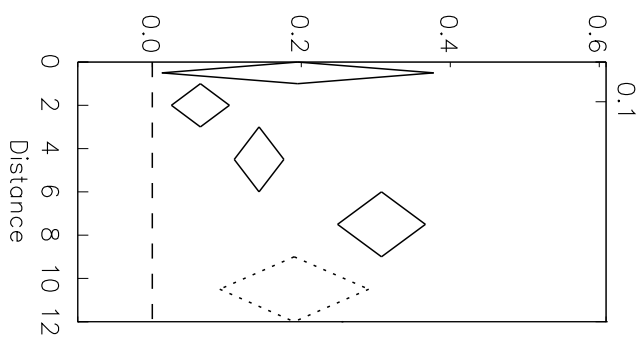
A2219



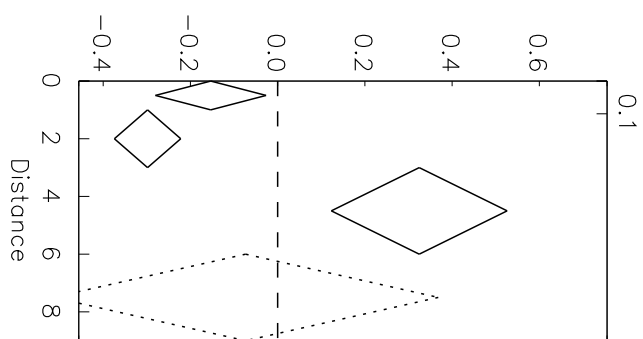
A3301



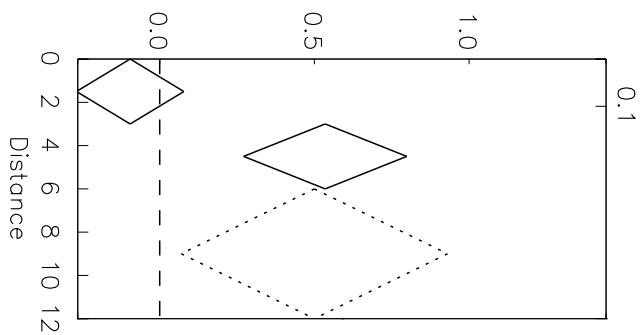
A2597



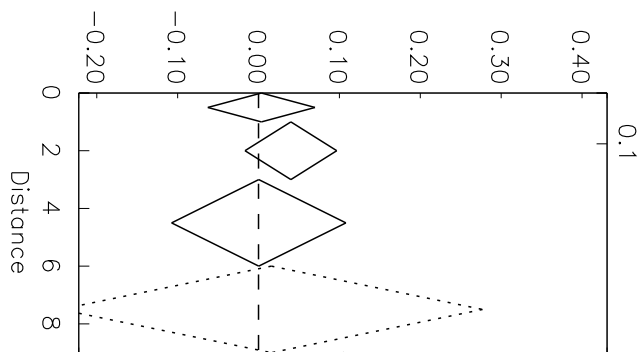
A3558



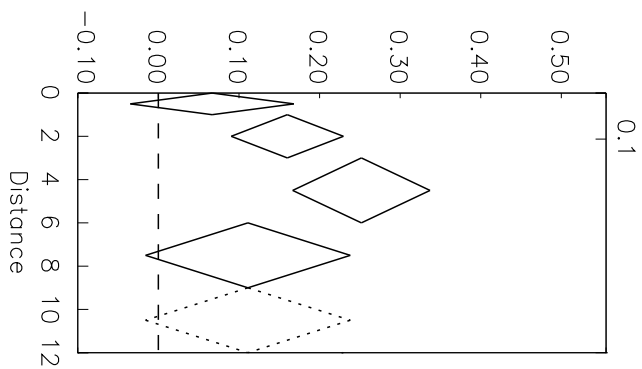
A2670



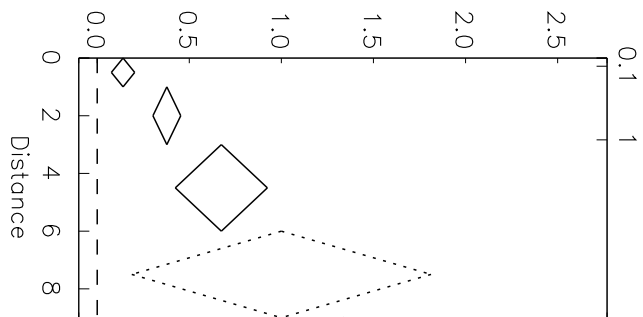
A3560



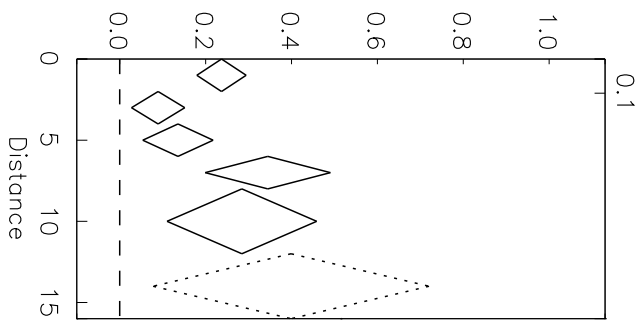
A2717



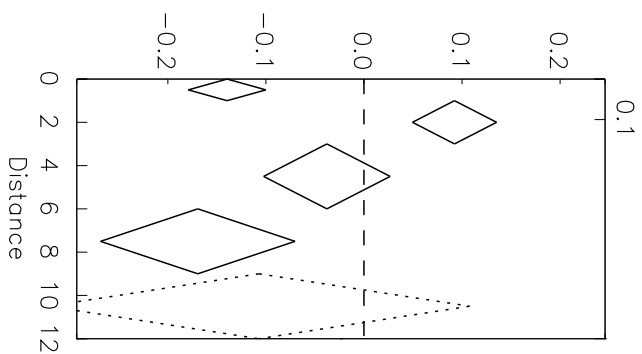
A3562



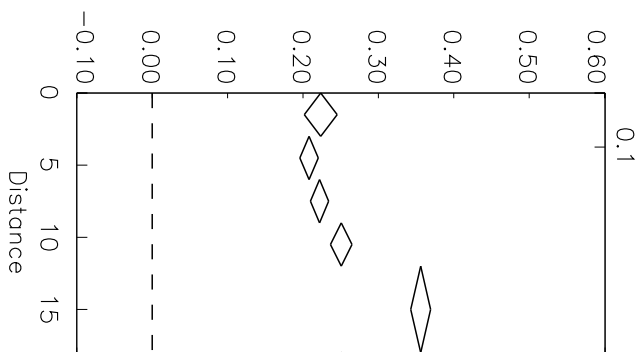
A2744



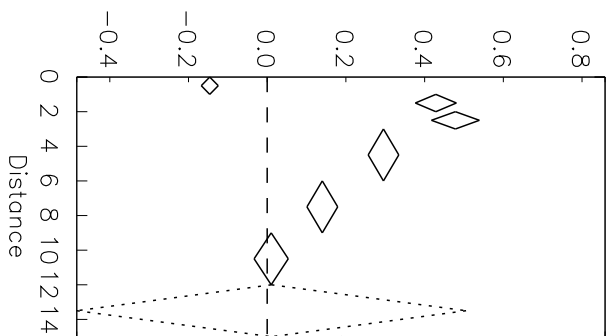
A3571



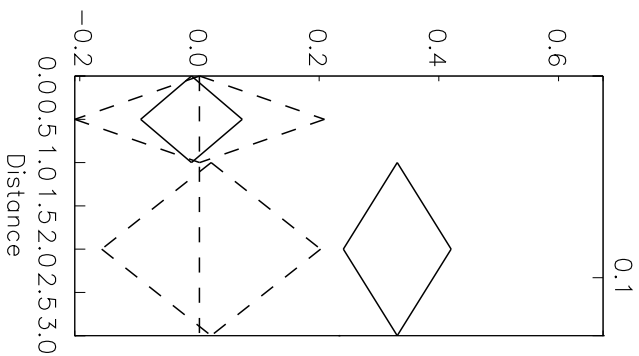
A4059



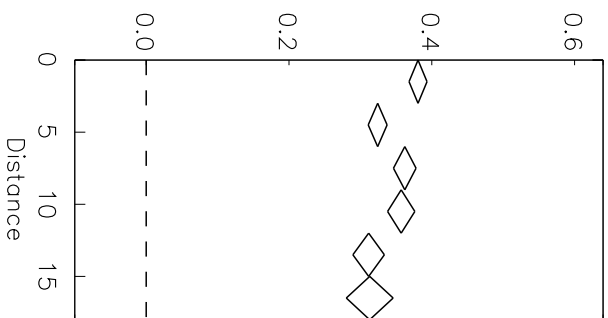
Coma



Fornax



Hercules



Virgo

